ORP5 REGULATES TRANSPORT OF LIPIDS AND CALCIUM TO MITOCHONDRIA AT ENDOPLASMIC RETICULUM-MITOCHONDRIA MEMBRANE CONTACT SITES

Leila Rochin[1], Cécile Sauvanet[1]*, Eeva Jääskeläinen[2]*, Audrey Houcine[3]*, Annukka Kivelä[2], Xingjie MA[5], Eyra Marien[4], Jonas Dehairs[4], Julie Neveu[1], Romain Le Bars[1], Johannes Swinnen[4], David Bernard[5], David Tareste[6], Vesa M. Olkkonen[2,7], and Francesca Giordano[1#]

[1] Institute for Integrative Biology of the Cell (I2BC), CEA, CNRS, Univ. Paris-Sud, Université Paris-Saclay, Gif-sur-Yvette cedex 91198, France.

[2] Minerva Foundation Institute for Medical Research, Biomedicum 2U, FI-00290 Helsinki, Finland

[3] Institut Jacques Monod, CNRS, UMR7592, Université Paris Diderot, Sorbonne Paris Cité, F-75013 Paris, France

[4] Laboratory of lipid metabolism and cancer, Department of Oncology, KU Leuven, Leuven B-3000, Belgium.

[5] Centre de Recherche en Cancérologie de Lyon, UMR INSERM U1052/CNRS 5286, Centre Léon Bérard, 69373 LYON Cedex 08, France

[6] Institute of Psychiatry and Neuroscience of Paris (IPNP), UMR-S1266 INSERM-Paris Descartes University, Paris, France

[7] Department of Anatomy, Faculty of Medicine, FI-00014 University of Helsinki, Finland

* These authors contributed equally to this work

[#] Correspondence to: francesca.giordano@i2bc.paris-saclay.fr

ABSTRACT

Mitochondria are dynamic organelles essential for cell survival whose structural and functional integrity rely on selective and regulated transport of lipids from/to the endoplasmic reticulum (ER) and across the two mitochondrial membranes. As they are not connected by vesicle transport, the exchange of lipids between ER and mitochondria occurs at sites of close organelle apposition called membrane contact sites. However, the mechanisms and proteins involved in these processes are only beginning to emerge. Here, we show that ORP5/8 mediate non-vesicular transport of Phosphatidylserine (PS) from the ER to mitochondria in mammalian cells. We also show that ER-mitochondria contacts where ORP5/8 reside are physically and functionally linked to the MIB/MICOS complexes that bridge the mitochondria membranes, cooperating with them to facilitate PS transfer from the ER to the mitochondria. Finally, we show that ORP5 but not ORP8, additionally regulates import of calcium to mitochondria and consequently cell senescence.

KEYWORDS

Membrane contact sites, mitochondria, ORP, lipid transfer, calcium

ABBREVIATIONS

APOO: Apolipoprotein O

APOOL: Apolipoprotein O-like

CHCHD3/6: Coiled-Coil-Helix-Coiled-Coil-Helix Domain Containing 3/6

Calcium: Ca^{2+}

CCCP: Carbonyl cyanide 3-chlorophenylhydrazone

CJ: cristae junctions

CV-ATP5A: complex V alpha subunit

EM: electron microscopy

ER: endoplasmic reticulum

FFAT: two phenylalanines (FF) in an Acidic Tract

GRP75: glucose-regulated protein 75

HRP: horseradish peroxidase

IF: immunofluorescence

IMM: inner mitochondrial membrane

IMS: intermembrane space

IP3R: Inositol trisphosphate receptor

LAR-GECO: low-affinity red fluorescent genetically encoded Ca2+ indicators for optical imaging

LTPs: lipid transfer proteins

MAM: mitochondria-associated ER membrane

MCU: mitochondrial calcium uniporter

MIB: Mitochondrial intermembrane space bridging complex

MICOS: Mitochondrial Contact Sites and Cristae Junction Organizing System

MINOS1: mitochondrial inner membrane organizing system 1

76 MS: mass spectrometry

77 mt-Pericam: mitochondrial permuted YFP and a CaM (calmodulin)

78 OMM: outer mitochondrial membrane

79 ORD: OSBP-related lipid-binding/transfer domain

80 ORP: Oxysterol binding protein (OSBP)-related proteins

81 Osh: oxysterol-binding homology

82 PC: Phosphatidylcholine

83 PDI: Protein disulfide isomerase

84 PE: phosphatidylethanolamine

85 PH: pleckstrin homology

86 PI4P: Phosphatidylinositol-4-phosphate

87 PIP2: Phosphatidylinositol 4,5-bisphosphate

88 POPC: Palmitoyloleoylphosphatidylcholine

89 PS: phosphatidylserine

90 PTPIP51: Protein tyrosine phosphatase interacting protein 51

91 QIL1: MICOS complex subunit MIC13

92 R-GECO: Red fluorescent, genetically-encoded Ca2+ indicator for optical imaging

93 SA β-gal: Senescence-associated β –galactosidase

94 SAM: Sorting and Assembly Machinery

95 SAM50: Sorting Assembly Machinery 50

96 TLC: thin layer chromatography

97 TMRE: Tetramethylrhodamine ethyl ester

98 VAPB: Vesicle-associated membrane protein-associated protein B

99 VDAC: Voltage Dependent Anion Channel

100 WB: western blotting

INTRODUCTION

Vesicular trafficking is the major pathway for transport of proteins and metabolites, such as lipids, between membranes. However, an alternative route, which is vesicle-independent, occurs at regions of close inter-organelle membrane proximity (within less than 30 nm) also called membrane contact sites (Scorrano, De Matteis et al., 2019). This route is particularly important to preserve membrane composition, integrity and identity of the intracellular organelles such as the mitochondria that are largely excluded from the classical vesicle-mediated trafficking pathways. Like other organelles, mitochondria can be closely associated with the endoplasmic reticulum (ER), the major site of lipid synthesis and the major intracellular calcium (Ca^{2+}) store. ER membrane subdomains closely apposed to the mitochondria are called mitochondria-associated ER membranes (MAMs) and they facilitate the exchange of Ca^{2+} and lipids between the two organelles (Herrera-Cruz & Simmen, 2017, Tatsuta, Scharwey et al., 2014, Vance, 2014)

Mitochondria are involved in a plethora of cellular processes including energy production, lipid metabolism, Ca^{2+} homeostasis and apoptosis. To fulfill their numerous functions, mitochondria need to maintain a defined membrane composition by receiving essential lipids and lipid precursors from the ER through membrane contact sites (Giordano, 2018, Vance & Tasseva, 2013).

Increasing lines of evidence suggest that lipid transfer proteins (LTPs) play a major role in regulating the lipid composition of membranous organelles by facilitating non-vesicular lipid transport at membrane contact sites. In recent years, several tethering complexes with lipid transfer activity have been identified at membrane contact sites between the ER and other intracellular organelles including the plasma membrane (PM) in yeast as well as in mammalian cells. However, the LTPs of ER-mitochondria

126 membrane contact sites remain still mysterious. The best-studied lipid transfer/tethering
127 complex at ER-mitochondria contact sites is the yeast ER-mitochondria encounter
128 structure (ERMES) (Kornmann et al 2009, Lang et al 2015) that bridges the ER and
129 the mitochondrial membranes and also facilitates the exchange of phospholipids (in
130 particular phosphatidylcoline, PC) between them. Despite its important functions in
131 yeast, the ERMES complex is not conserved in metazoans. In metazoans, very little
132 is known on how lipids are exchanged at ER-mitochondria membrane contact sites
133 and about the proteins involved in this process. Some tethers at mammalian ER-
134 mitochondria contact sites have started to emerge in the past years (Gatta and
135 Levine 2017), including the Mitochondrial Ca^{2+} Uniporter (MCU)–Voltage Dependent
136 Anion Channel (VDAC)–Glucose Regulated Protein 75 (GRP75)–Inositol
137 Triphosphate Receptor (IP3R) machinery involved in Ca^{2+} import from the ER to
138 mitochondria (Rizzuto et al. 2009) and the recently identified Protein tyrosine
139 phosphatase interacting protein 51 (PTPIP51)–Vesicle-associated membrane
140 protein-associated protein B (VAPB) complex (Stoica et al 2014) alteration of which
141 induces defects in ER-mitochondria tethering and Ca^{2+} exchanges. However, none of
142 these proteins has been directly involved in non-vesicular lipid transport between ER
143 and mitochondria membranes.

144 The Oxysterol binding protein (OSBP)-related proteins constitute a large family of
145 LTPs conserved from yeast (Osh) to humans (ORP) and localized to different
146 subcellular sites, shown in several cases to be membrane contact sites. A common
147 feature of all ORPs is the presence of an OSBP-related lipid-binding/transfer (ORD)
148 domain. Most ORP proteins contain an FFAT domain that binds ER-localized VAP
149 proteins and a pleckstrin homology (PH) domain that interacts with lipids or proteins
150 in distinct non-ER organelle membranes. Two members of this family, ORP5 and

151 ORP8, do not contain a FFAT domain but are directly anchored to the ER through
152 their C-terminal domain. We have recently shown that ORP5 and ORP8 localize to
153 ER-mitochondria contact sites where they play a key role in maintaining
154 mitochondrial morphology and respiratory function (Galmes et al. 2016). ORP5 and
155 ORP8 have been previously shown to transfer phosphatidylserine (PS) from the
156 cortical ER to the PM, in counter-exchange with the phosphoinositides
157 Phosphatidylinositol-4-phosphate (PI4P) and Phosphatidylinositol 4,5-bisphosphate
158 (PIP_2) (Chung et al. 2015; Ghai et al, 2017). Interestingly, transport of PS occurs also
159 at ER-mitochondria contact sites. Newly synthesized PS, by the ER-localized PS-
160 Synthase 1 (PSS1), is shuttled from the ER to the outer mitochondrial membrane
161 (OMM) and from OMM to inner mitochondrial membrane (IMM) where it is rapidly
162 converted to phosphatidylethanolamine (PE) (Vance, 1990, Vance & Tasseva, 2013). At
163 the IMM, PE plays crucial roles in maintaining mitochondrial tubular morphology and
164 therefore in mitochondrial respiratory functions (Joshi, Thompson et al., 2012,
165 Steenbergen, Nanowski et al., 2005). Regardless of extensive studies on PS transport
166 between ER and mitochondria since its first discovery more than 20 years ago (Vance,
167 1990), the mechanisms underlying this transport and the proteins involved are still
168 elusive.

169 Here we show that ORP5 and ORP8 are the LTPs that transfer PS from the ER
170 to the mitochondria at ER-mitochondria contact sites in mammalian cells. We also
171 show that they are physically and functionally connected with Sorting Assembly
172 Machinery 50 (SAM50) and Mitofilin, two components of the Mitochondrial
173 Intermembrane space Bridging (MIB) and Mitochondrial Contact sites and Cristae
174 junction Organizing System (MICOS) complexes, that anchors the IMM to the OMM.
175 The MICOS complex (composed of seven proteins: Mitofilin, CHCHD3, CHCHD6,

176 APOO, QIL1, APOOL and MINOS1) is preferentially located at Cristae Junctions (CJ),
177 tubular structures that connect the IMM to the cristae, and it is necessary for CJ
178 formation, cristae morphology and mitochondria function (Harner, Korner et al., 2011,
179 Huynen, Muhlmeister et al., 2016, Ott, Dorsch et al., 2015, Wollweber, von der
180 Malsburg et al., 2017). The integral IMM protein Mitofilin is the central component of
181 the MICOS complex and carries a large domain exposed to the mitochondria
182 intermembrane space (IMS) that interacts with the OMM Sorting and Assembly
183 Machinery (SAM) to form the MIB complex (Friedman, Mourier et al., 2015, Guarani,
184 McNeill et al., 2015). The SAM complex is constituted of SAM50 (a pore-forming β-
185 barrel protein), Metaxin1 and 2, and is involved in the membrane insertion and
186 assembly of mitochondrial β-barrel proteins (Hohr, Lindau et al., 2018, Kozjak,
187 Wiedemann et al., 2003, Kozjak-Pavlovic, Ross et al., 2007) (see cartoon in Figure
188 8).

189 Here we show that ORP5/8 interact and cooperate with SAM50 and Mitofilin to
190 facilitate the movement of PS from the ER to the mitochondria across ER-
191 mitochondria contact sites and the IMS and consequently the synthesis of
192 mitochondrial PE. Finally, we uncover an additional role for ORP5, but not ORP8, in
193 regulating Ca^{2+} import to mitochondria, through regulation of SAM50-VDAC protein
194 levels. Our findings reveal a novel link between lipid and Ca^{2+} transport at ER-
195 mitochondria contact sites and provide a mechanistic insight of the specific role of
196 ORP5 in modulating cellular senescence.
197
198
199
200

201 **RESULTS**

202 **ORP5 and ORP8 transport PS from the ER to the mitochondria at ER-**
203 **mitochondria contact sites**

204 We have recently reported that ORP5 and ORP8, shown to transfer lipids at ER-PM
205 contacts, localize also to ER-mitochondria contact sites (Galmes, Houcine et al., 2016).
206 However, their role in lipid transport at ER-mitochondria contacts still remains to be
207 established. Taking into account their role in counter-exchanging PS with the PM
208 phosphoinositides PI4P and PIP_2 at ER-PM contacts (Chung et al. 2015; Ghai et al,
209 2017), we hypothesized that ORP5 and ORP8 could also mediate PS transport at ER-
210 mitochondria contact sites.

211 The ORD domain of ORP8 has been shown to transfer PS (in counter-transport
212 with PI4P or PIP_2) between liposome membranes *in vitro* (Chung et al. 2015; Ghai et
213 al, 2017). Since PI4P and PIP_2 are not present on mitochondrial membranes it is
214 possible that at ER-mitochondria contact sites ORP5/8 might transport back to the
215 ER other phospholipids, such as PE. However, no study so far has ever addressed
216 the ability of ORP5 and ORP8 ORD domains (ORD5, ORD8) to transfer other
217 phospholipids between liposomes *in vitro.* First, to compare and study the role of
218 ORD5 and ORD8 in the transfer of phospholipids *in vitro*, we purified the recombinant
219 ORD5 (aa 265-703) and ORD8 (aa 328-767) in bacteria (Escherichia coli) (Fig. S1a)
220 and analyzed their lipid transfer ability by measuring the transport of fluorescent
221 phospholipids (TopFluor-PS, -PC or -PE) from donor to acceptor liposomes *in vitro*.
222 Donor liposomes containing fluorescent phospholipids and biotinylated lipids
223 (liposomes composed of 1 mol% TopFluor-PS, -PC or -PE and 2 mol% of
224 biotinylated-PE, and 97 mol% POPC) were first immobilized on streptavidin beads
225 and then mixed with acceptor liposomes (composed of 100 mol % POPC) in

226 presence or absence of ORP5/8 ORD domains (Fig. 1a). After 1 hour at 37°C,
227 acceptor liposomes were recovered from the supernatant and their fluorescence was
228 measured (Fig. 1a). Our results show that both ORD5 and ORD8 transfer PS, but not
229 PC and PE, from donor to acceptor liposomes (Fig. 1b). They also reveal that ORD5
230 and ORD8 share equivalent abilities to transfer PS *in vitro*.

231 Next, we addressed whether ORP5 and ORP8 could mediate non-vesicular
232 transfer of PS at ER-mitochondria contact sites *in situ*. As the ER-derived PS is the
233 major precursor for mitochondrial PE, if ORP5 and ORP8 mediate non-vesicular
234 transport of PS from the ER to the mitochondria, then their absence should lead to a
235 reduction of mitochondrial PE. To test this, we used Percoll gradient-based
236 subcellular fractionation (Galmes et al. 2016) to isolate pure mitochondria from HeLa
237 cells where ORP5 or ORP8 were transiently silenced by RNAi. We chose to use a
238 transient knockdown as it overcomes the limits and/or compensatory effects on lipid
239 transport/biosynthetic pathways that other stable approaches could induce. The
240 purity of mitochondria and of the other subcellular fractions was verified in control,
241 ORP5 and ORP8 knockdown conditions by western blotting (WB) (Fig. S1b). As
242 controls for the purity of subcellular fractions, the samples were probed for
243 cytochrome c as mitochondrial marker and IP3R-3 as a MAM-enriched marker. All
244 markers were highly enriched in their respective fractions and were absent in the
245 others. In accord with our previous study (Galmes et al., 2016), ORP5 and ORP8
246 were enriched in the MAM fraction and absent in the mitochondria fraction of control
247 cells. On the contrary, they were strongly suppressed in ORP5 and ORP8
248 knockdown cell lysates and in the respective MAM fractions (Fig. S1b). The PE
249 content of purified mitochondria from ORP5 and ORP8 knockdown was then
250 analyzed by mass spectrometry (MS)-based lipidomics, revealing a reduction of PE

levels in mitochondria isolated from ORP5 and ORP8 knockdown cells of 34% and 20%, respectively, as compared to control cells (Fig. 1c). Interestingly, PE levels of the total cells were unchanged, indicating a specific effect of ORP5 or ORP8 depletion on mitochondrial PE.

In subsequent experiments, we measured the levels of mitochondrial PE newly synthesized from the ER-derived PS by using a radiometric PS-to-PE conversion assay *in situ* (Shiao, Lupo et al., 1995) in silenced or control HeLa cells (Fig. S1c-1d). This assay allows the monitoring of PS transfer from the ER to mitochondria by measuring the levels of radioactive PS and PS-derived PE by thin layer chromatography (TLC) after 18h of incorporation of radioactive L-[^{3}H(G)]-serine into the cells. A significant decrease in the levels of newly synthetized PE was found in ORP5 knockdown and in ORP5+ORP8 double-knockdown cells (Fig. 1d). The decrease was stronger in ORP5+ORP8 double-knockdown cells, indicating a cooperative effect of ORP5 and ORP8 in this process. A slight decrease was also found in ORP8 knockdown cells, although not statistically significant, suggesting a major role of ORP5 compared to ORP8 in PS transfer at ER-mitochondria contact sites *in situ*.

The decrease in mitochondria PE is in accord with its essential role in maintaining the morphology of mitochondrial cristae and with our previous electron microscopy (EM) observations that knockdown of ORP5 or ORP8 alters the architecture of the cristae, while ER-mitochondria contact sites with normal morphology were still visible (Galmes et al., 2016). However, our previous study did not rule out that these contact sites could be affected in their number/size. To test whether the effects on PS transport at ER-mitochondria contacts were specific of ORP5 and ORP8 loss of function or simply due to a decrease of ER-mitochondria

276 contacts induced by their knockdown, we quantified the abundance of ER-
277 mitochondria contact sites by EM in control and ORP5, ORP8, ORP5+ORP8
278 knockdown cells. To facilitate the visualization of the ER we transfected the cells with
279 a HRP-KDEL construct (carrying a horseradish peroxidase (HRP) tagged with an ER
280 retention motif) that stains the ER with a dark signal. Our quantifications revealed
281 that ORP5, ORP8 or ORP5+ORP8 knockdowns did not affect the extent of ER-
282 mitochondria contact sites (Fig. 1e-1f). These results indicate that ORP5 and ORP8
283 silencing affect non-vesicular PS transport at ER-mitochondria contacts but not their
284 extent and integrity, confirming that at these sites ORP5 and ORP8 act exclusively as
285 LTPs and not as tether (Fig. 1h). Additionally, 52% of mitochondria in ORP5+ORP8
286 double-knockdown cells display aberrant cristae morphology versus 9% in control
287 cells (Fig. 1e-1g). These defects in cristae morphology were stronger than what we
288 had previously shown in the case of ORP5 and ORP8 individual knockdowns
289 (Galmes et al., 2016), and most likely reflect the stronger effect of ORP5+ORP8
290 double-knockdown on PS transport at ER-mitochondria contact sites.
291
292 **ER-mitochondria contact sites marked by ORP5/8, are physically and**
293 **functionally connected with the mitochondrial intermembrane space bridging**
294 **(MIB) complex**
295 To investigate whether ORP5/8 localize to specific ER-mitochondria contact site
296 subdomains we performed a morphological analysis of ORP5 localization by
297 immuno-EM (IEM) on ultrathin cryosections from HeLa cells transfected with HA-
298 ORP5. The advantage of analyzing ORP5 localization is its preferential localization to
299 contact sites as compared to ORP8 (Galmes et al. 2016), which remains also largely
300 present within the reticular ER. Interestingly, the majority of ORP5 gold particles was

301 found to localize to ER elements in a very close proximity (86% within 0-100 nm
302 distances, 50% of which within 50 nm) to the CJ (arrow, Fig. 2a-b), tubular structures
303 that connect the IMM to the cristae. In yeast, CJ were shown to be closely associated
304 to OMM-IMM contact sites tethered by the MICOS complex (Harner et al., 2011). IEM
305 analysis using Mitofilin-EGFP, an EGFP-tagged construct of the human orthologue of
306 the central component of the MICOS complex, confirmed that human Mitofilin,
307 similarly to its yeast orthologue, preferentially localizes to the IMM in close proximity
308 of CJ and in the cristae that arise from them (arrow, Fig. 2a).

309 To identify specific binding partners of ORP5 at ER-mitochondria contact sites
310 we carried out a MS-analysis on GFP-pull downs from cells expressing EGFP-ORP5,
311 EGFP-ORP5ΔPH (an ORP5 mutant lacking the PM-targeting PH domain that is
312 localized at ER-mitochondria but not at ER-PM contact sites), or EGFP alone as a
313 control (Fig. S2a). As expected, the highest hit detected in both EGFP-ORP5 and
314 EGFP-ORP5ΔPH pull-downs was its binding partner ORP8, with which ORP5 forms
315 a complex at contact sites (Chung, Torta et al., 2015, Galmes et al., 2016). Other
316 major hits are listed in Fig. S2a and comprise several outer mitochondrial membrane
317 proteins, including the mitochondrial outer membrane protein PTPIP51, a previously
318 reported interacting partner of ORP5 (Galmes et al., 2016).

319 Interestingly, among these proteins the Sorting Assembly Machinery Subunit 50
320 (SAM50), a central component of the SAM protein complex involved in the import
321 and assembly of mitochondria β-barrel proteins in the OMM (Hohr et al., 2018), had
322 one of the highest scores. SAM50 is part of the Mitochondrial intermembrane space
323 bridging (MIB) complex, composed of metaxin-1, metaxin-2 and the MICOS complex
324 that anchors the OMM to the IMM at CJ (Huynen et al., 2016, Ott et al., 2015).
325 SAM50 is also known to directly bind the central component of the MICOS complex

326 Mitofilin (Ott et al., 2015). Consistently, Mitofilin was also detected in the MS of
327 EGFP-ORP5 and EGFP-ORP5ΔPH pull-downs (Fig. S2a). Interestingly, SAM50 and
328 Mitofilin showed a higher interaction score in EGFP-ORP5ΔPH immunoprecipitates,
329 as compared to EGFP-ORP5. Of note, metaxin-2, another component of the MIB
330 complex, localized to the outer mitochondrial membrane, was also detected in the
331 MS of immunoprecipitated EGFP-ORP5ΔPH, whereas its score in the EGFP-ORP5
332 was lower than the assigned threshold (50) (Fig. S2a). To verify that the
333 overexpression of ORP5 or ORP5ΔPH did not affect the protein levels of SAM50 and
334 Mitofilin, WB analysis using anti-actin as loading control was carried out on cells
335 expressing EGFP-ORP5, EGFP-ORP5ΔPH or EGFP alone. Our results show that
336 neither EGFP-ORP5 nor EGFP-ORP5ΔPH overexpression alters the amount of
337 SAM50 and Mitofilin proteins as compared to the overexpression of EGFP alone (Fig.
338 S2b).

339 To confirm ORP5/8 interaction with SAM50 and Mitofilin, GFP-pull down
340 experiments from HeLa cells expressing EGFP-ORP5, EGFP-ORP8 or EGFP alone
341 were carried out (Fig. 2d). Consistent with the MS data, endogenous SAM50 and
342 Mitofilin were recovered with both EGFP-ORP5 and EGFP-ORP8 but not with EGFP
343 alone, confirming specific interaction of ORP5 and ORP8 with SAM50 and Mitofilin.
344 Of interest, the interaction of SAM50 and Mitofilin with EGFP-ORP5 was stronger
345 than with EGFP-ORP8.

346 Parallel GFP-pull down experiments were carried out from cells expressing
347 EGFP-tagged ORP5 (EGFP-ORP5ΔPH) or ORP8 (EGFP-ORP8ΔPH) PH domain
348 deleted constructs, and compared to the full-length proteins (EGFP-ORP5 and
349 EGFP-ORP8) or to the EGFP alone. In accord with the MS data, the deletion of the
350 PH domain increased ORP5 interaction with SAM50, as compared to the full-length

351 protein (Fig. 2e). In addition, EGFP-ORP8ΔPH interaction with SAM50 was higher
352 than of EGFP-ORP8, although still lower than the interaction of EGFP-ORP5ΔPH or
353 even EGFP-ORP5 with SAM50.

354 As the PH domain is not required for the interaction with SAM50 we further
355 investigated the role of the other domains of ORP5 in such interaction by
356 immunoprecipitating ORP5 deletion mutants for the ORD and the transmembrane
357 (TM) domains (EGFP-ORP5ΔORD, EGFP-ORP5ΔTM). While the deletion of the
358 ORD domain did not affect the interaction between ORP5 and SAM50, the deletion of
359 the TM domain decreased the amount of SAM50 co-immunoprecipitated with ORP5,
360 indicating that ORP5 should be properly anchored to the ER to localize at ER-
361 mitochondria contact sites and to interact with SAM50 (Fig. 2d).

362 To observe ORP5 and SAM50 localization we performed confocal analysis on
363 cells expressing EGFP-ORP5 or EGFP-ORP5ΔPH and stained with an anti-SAM50
364 antibody to look at the endogenous protein (Fig. 2e). As expected, endogenous
365 SAM50 localizes on mitochondria in cells stained with Mitotracker and, as previously
366 shown (Galmes et al., 2016), EGFP-ORP5 localizes to both ER-PM and ER-
367 mitochondria contact sites while the EGFP-ORP5ΔPH loses its localization to ER-PM
368 contacts. Both full-length and ΔPH constructs co-localized with endogenous SAM50
369 at ER elements in contact with mitochondria (Fig. 2e). However, this was more
370 evident in the case of EGFP-ORP5ΔPH (bottom image, Fig. 2e).

371 To test whether ORP5 and the MIB complex functionally cooperate in non-
372 vesicular transfer of PS we depleted ORP5, SAM50 or Mitofilin alone or in
373 combination by RNAi and analyzed the content in mitochondrial PE newly
374 synthesized from PS using the same radiometric PS-to-PE conversion assay *in*
375 *situ* described above. Robust knockdown of ORP5, SAM50 or Mitofilin was

376 confirmed by western blotting after 48 hours (Fig. 3a). Analysis of PS-derived
377 newly synthetized PE revealed a significant decrease in PE in ORP5 (Fig. 1d and
378 Fig. 3b) and Mitofilin knockdown cells (Fig. 3b). Moreover, the double-knockdown
379 of ORP5 and Mitofilin had an additive effect, supporting a cooperative function of
380 these two proteins in the same process (PS transport/PE synthesis). However, the
381 levels of PE were not changed in SAM50 knockdown cells as compared to control.
382 This can be explained by the fact that other subunits of the MIB complex (i.e.
383 Mitofilin) might compensate for its depletion. Indeed, levels of Mitofilin are
384 increased in SAM50 knockdown cells (Fig. 3a). Accordingly, the double-silencing
385 of SAM50 and either ORP5 or Mitofilin had a significant impact on PE synthesis
386 (Fig. 3b). Moreover, the reduction in PE was even stronger as compared to the
387 individual knockdowns indicating that disruption of two components of PS
388 transport pathways (*via* direct transport at ER-mitochondria contact sites and/or
389 *via* OMM-IMM tethering) has a significant impact on PE synthesis.

390 To verify the possibility of an indirect effect of Mitofilin or SAM50 silencing on the
391 morphology and abundance of ER-mitochondria contacts we carried out a
392 morphological analysis by conventional EM in all these knockdown conditions and
393 quantified ER-mitochondria contacts by HRP-KDEL EM (to stain the ER) in Mitofilin
394 or SAM50 silenced cells. Morphological analysis by conventional EM showed that
395 transient (48 hours) knockdowns of SAM50 and Mitofilin, as well as double-
396 knockdowns of ORP5+Mitofilin, ORP5+SAM50 and SAM50+Mitofilin, induce
397 formation of multilamellar cristae, almost devoid of CJ (Fig. S3a-b), complementing
398 previous observations obtained by other groups through stable disruption of the
399 MICOS/MIB functions (Ding, Wu et al., 2015, Ott et al., 2015). However, in all
400 knockdown conditions analyzed ER-mitochondria contact sites were still present and

401 their morphology not altered. Quantitative morphological analysis by HRP-KDEL EM
402 in control and Mitofilin or SAM50 silenced cells confirmed that the abundance of ER-
403 mitochondria contact sites was not altered by Mitofilin or SAM50 knockdown (Fig. 3c-
404 d) indicating that the effects on PS-derived PE synthesis were specifically due to
405 Mitofilin or SAM50 loss of function effects on intra-mitochondrial membrane bridges.
406 Overall our results indicate that ER-mitochondria contacts where ORP5/8 localize
407 are physically and functionally linked to intra-mitochondria contacts where the
408 components of the MIB/MICOS complex reside, and this association facilitates the
409 transfer of PS from the OMM to the IMM for synthesis of PE.
410

411 **ORP5 additionally regulates VDAC-mediated Ca^{2+} import to mitochondria**
412 **through its interaction with SAM50**

413 To get further insights into the functional link between ORP5/8 and the
414 MIB/MICOS complex we explored whether ORP5 and ORP8 knockdowns might
415 affect the expression and/or the localization of SAM50 and Mitofilin. Interestingly
416 when we analyzed cell lysates by WB, we found that SAM50 and Mitofilin protein
417 expression was significantly and specifically increased in ORP5- but not in ORP8
418 knockdown cells, as compared to control cells (Fig. 4a-b). The effects of ORP5
419 silencing were specific for SAM50 and Mitofilin, as other mitochondrial proteins
420 (Cytochrome c, CV-ATP5A) or proteins of the general ER (PDI) and of the MAMs
421 (VAPB) were not affected (Fig. S2c). This could also be observed by IF analysis
422 where the increase in SAM50 staining is specific to ORP5 knockdown (Fig. 4c).
423 Intriguingly, such increase in SAM50 was accompanied by a dramatic
424 accumulation in the voltage-dependent anion channel VDAC, a 19-stranded
425 transmembrane β-barrel protein (Colombini, 2012) that requires SAM50 for its

426 biogenesis and insertion in the OMM (Hohr et al., 2018). These results suggest that the
427 accumulation of VDAC protein in ORP5 knockdown cells is due to the parallel
428 increase of SAM50. The simultaneous knockdowns of ORP5 and SAM50 rescued
429 the increase in VDAC, confirming that its accumulation in ORP5 knockdown cells
430 was due to the accumulation of SAM50. Interestingly, ORP5 and SAM50 double-
431 knockdown did not rescue the increased protein levels of Mitofilin (Fig. 4a-b), in
432 accord with the fact that SAM50 knockdown alone also increased the protein levels
433 of Mitofilin. To verify that the increase in their protein amounts did not depend on the
434 increase in their transcripts we quantified the transcript levels of ORP5, SAM50 and
435 the three VDAC isoforms (VDAC1, 2 and 3) by real-time PCR upon ORP5 or SAM50
436 knockdown (Fig. 4d). The quantity of SAM50 and Mitofilin transcripts was unaffected
437 by ORP5 silencing, and VDAC1 transcript levels were even slightly reduced, possibly
438 reflecting a compensatory mechanism induced by the increase in VDAC protein.
439 Similarly, ORP5, VDAC and Mitofilin transcript levels were not affected in the
440 absence of SAM50. Overall, these data indicate that ORP5 knockdown induces an
441 accumulation of SAM50 and VDAC (SAM50-dependent) proteins in the absence of
442 major effects on the corresponding mRNAs.

443 As VDAC is one of the major mitochondrial players in mediating Ca^{2+} transport
444 and signaling between ER and mitochondria (Rapizzi, Pinton et al., 2002), we next
445 investigated if ORP5 knockdown could regulate Ca^{2+} influx from the ER to
446 mitochondria in living cells. We first used a ratiometric Ca^{2+} indicator selectively
447 targeted to mitochondria (mt-Pericam) which is based on a circularly permuted yellow
448 fluorescent protein fused to calmodulin (Nagai, Sawano et al., 2001). Upon binding to
449 Ca^{2+}, the excitation peak of mt-Pericam shifts from 415 nm to 494 nm while the
450 emission spectrum remains unchanged at 515 nm, allowing us to quantify rapid

451 changes in mitochondrial Ca^{2+}. We thus transfected ORP5, ORP8 or Ctrl siRNA-
452 treated cells with mt-Pericam and then we measured mitochondrial Ca^{2+} fluxes, in
453 response to histamine, by live-cell spinning disk microscopy (Fig. 5a-b). Soon after
454 the addition of histamine mt-Pericam fluorescence ratio (488/405) rapidly increased
455 in all conditions, reflecting the increase in mitochondrial Ca^{2+} influx triggered by the
456 histamine treatment. However, interestingly, ORP5 knockdown cells showed a
457 significantly higher increase as compared to ORP8 knockdown and to control cells.
458 Quantification of the maximum amplitude of the response after histamine treatment
459 (expressed as R_{max}/R_0, where R is the 488/405 ratio, R_{max} is the maximum
460 fluorescence ratio after histamine addition and R_0 the basal ratio before histamine
461 addition) confirmed that ORP5 but not ORP8 silencing induced a statistically relevant
462 increase of mitochondrial Ca^{2+} influx, triggered by the addition of histamine, as
463 compared to control cells (Fig. 5b).

464 Passive entry of Ca^{2+} into mitochondria can be driven by large negative
465 membrane potential of mitochondria and occurs through the mitochondrial Ca^{2+}
466 uniporter MCU spanning the IMM (Patron, Raffaello et al., 2013). To be sure that the
467 increase of mitochondrial Ca^{2+} upon ORP5 knockdown was not indirectly due to a
468 change of mitochondrial membrane potential, we performed flow cytometric analysis
469 in ORP5 or ORP8 knockdown cells. Knockdown cells were loaded with the
470 mitochondrial membrane potential sensitive dye TMRE (Tetramethylrhodamine ethyl
471 ester), in the presence (or absence) of the mitochondrial oxidative phosphorylation
472 uncoupler CCCP (Carbonyl cyanide 3-chlorophenylhydrazone) to induce membrane
473 depolarization (Fig. S4a). Neither ORP5 nor ORP8 knockdown altered mitochondrial
474 membrane potential as compared to control cells, even in presence of CCCP that
475 strongly decreases TMRE fluorescence intensity (Fig. S4a), showing that the effect of

476 ORP5 knockdown on Ca^{2+} is not due to a change of mitochondrial membrane
477 potential.

478 To further study the role of ORP5 in the regulation of Ca^{2+} homeostasis a parallel
479 set of experiments was performed using another type of Ca^{2+}-probe, the red
480 fluorescent genetically encoded Ca^{2+} indicator (R-GECO) and its two variants
481 selectively-targeted to mitochondria (mito-LAR-GECO) or ER (ER-LAR-GECO) to
482 respectively measure cytosolic, mitochondrial and ER Ca^{2+} in living cells (Fig. 5c-e).
483 These experiments confirmed that ORP5 silencing increases mitochondrial Ca^{2+}
484 uptake (Fig. 5c). The increase in mitochondrial Ca^{2+} uptake triggered by histamine
485 treatment was accompanied by a decrease in ER Ca^{2+} and an increase in cytosolic
486 Ca^{2+} in all conditions (Fig. 5d-e). Interestingly, no statistically relevant differences of
487 the decrease ER Ca^{2+} were measured between ORP5 silenced and control cells.
488 This indicates that the effects on mitochondrial Ca^{2+} fluxes observed in ORP5 do not
489 depend on the modification of ER Ca^{2+} storage or release. An increase in cytosolic Ca^{2+}
490 was measured in ORP5 and ORP8 silenced cells as compared to control. As this
491 increase was not specific of ORP5 silencing, it likely reflects a common role of
492 ORP5/8 in Ca^{2+} homeostasis at ER-PM contact sites, as recently proposed (Pulli,
493 Lassila et al., 2018).

494 So far, our data show that absence of ORP5 increases mitochondrial Ca^{2+}
495 possibly acting on the mitochondrial proteins SAM50 and VDAC and this is supported
496 by their specific accumulation in the absence of ORP5. To confirm that the increase
497 of mitochondrial Ca^{2+} in ORP5-silenced cells was indeed dependent on VDAC and
498 SAM50, we measured mitochondrial Ca^{2+} using mt-Pericam in VDAC- (all three
499 isoforms), ORP5+VDAC- and ORP5+SAM50- doubly-silenced cells. A significant
500 decrease in VDAC and SAM50 as well as ORP5 levels was detected by WB in the

501 corresponding silenced cells (Fig. 6a and Fig. 4a). Even though the increased level of
502 VDAC protein induced by the absence of ORP5 was not completely rescued in
503 ORP5+VDAC or ORP5+SAM50 knockdowns, the increase in mitochondrial Ca^{2+}
504 phenotype was significantly rescued to control levels and partially rescued in
505 ORP5+VDAC and ORP5+SAM50-silenced cells respectively (Fig. 6b and c). Overall,
506 these results demonstrated that ORP5 plays an additional role in regulating import of
507 mitochondrial Ca^{2+} through regulation of SAM50 and VDAC proteins.
508

509 **ORP5 knockdown induces cell senescence in a SAM50-dependent manner**

510 Accumulation of mitochondrial Ca^{2+} has been shown to be involved in both
511 apoptotic cell death and senescence (permanent cell proliferation arrest) (Wiel,
512 Lallet-Daher et al., 2014). Interestingly, it also has been shown that ORP5 expression
513 promotes cell proliferation (Du, Zadoorian et al., 2018). As our data show a new role
514 of ORP5 in regulating Ca^{2+} import to mitochondria at ER-mitochondria contact sites
515 (Fig. 6), we were wondering if ORP5 could mediate cellular processes such as
516 apoptosis and senescence. To address this question, we decided to study both
517 apoptosis and senescence in ORP5 depleted cells.

518 For apoptosis, we performed immunofluorescence and stained with anti-cleaved
519 caspase-3 (to detect apoptotic cells) HeLa cells transfected with control siRNA or
520 siRNA against ORP5 or ORP8. We also treated the knockdown cells with
521 staurosporine to induce apoptosis or with DMSO as control (Fig. S4b). Quantification
522 of the percentage of cleaved caspase-3 positive cells (% of total cells) in all
523 conditions showed no significant difference between ORPs knockdown and control
524 cells (Fig. S4b), even in presence of staurosporine, showing that in these conditions
525 (transient silencing) ORP5/8 are not mediating apoptosis.

526 To study cellular senescence we performed knockdown of ORP5 in MRC5
527 normal human fibroblasts that are a good model for senescence studies (Ma,
528 Warnier et al., 2018). We first looked at cell proliferation using crystal violet staining
529 in both control and ORP5 knockdown cells (Fig. 7a). A significant decrease of the cell
530 number was detected in ORP5 depleted cells compared to control (Fig. 7a). This
531 decrease of the cell number in ORP5 knockdown cells could be correlated with an
532 increase of the Senescence-associated β –galactosidase (SA β-gal) staining in this
533 condition as compared to control (Fig. 7a). Accordingly, these results were
534 corroborated by qRT-PCR analysis showing a significant increase of senescence
535 markers p16 and p21 and a significant decrease of the proliferation marker Ki67 in
536 ORP5 knockdown cells compared to control (Fig. 7b). Because we have shown that
537 ORP5 knockdown induces an elevation of mitochondrial Ca^{2+} via a SAM50-
538 dependent accumulation of VDAC, we hypothesized that the induction of senescence
539 in MRC5 cells was also due to the effect of ORP5 on SAM50. Thus, we decided to
540 perform a double-knockdown of ORP5 and SAM50 in MCR5 cells. In accord with our
541 hypothesis, double-silencing of ORP5 and SAM50 partially rescued the senescence
542 phenotype found in ORP5 knockdown cells. ORP5+SAM50 double-knockdown cells
543 displayed increased proliferation and underwent less senescence as compared to
544 ORP5 single knockdown cells (Fig. 7c). To verify that this effect on cellular
545 senescence was specific to ORP5, given its role on mitochondria Ca^{2+}, we performed
546 in parallel a knockdown of ORP8 in MRC5 cells. Differently to ORP5, ORP8
547 knockdown did not induce cell senescence (Fig. 7c). Taken together, these data
548 reveal a novel specific role of ORP5 and involving SAM50 in regulating cellular
549 senescence in MRC5 cells.
550

551 **DISCUSSION**

552 In this study, by using a combination of *in vitro* and *in situ* biochemical and imaging
553 approaches, we describe a new function of ORP5/8 in the maintenance of mitochondrial
554 levels of PE, an essential phospholipid of mitochondria, in mammalian cells. Importantly,
555 we provide the first evidence of LTPs (ORP5 and ORP8) directly mediating non-
556 vesicular transfer of PS at ER-mitochondria contact sites, from the ER to the
557 mitochondria where it is converted into PE.

558 In yeast, large complexes such as the ERMES and the ER-Membrane protein
559 Complex (EMC) have been previously involved in phospholipid trafficking (PC and
560 PS, respectively) between the ER and the mitochondrial membranes (Tamura &
561 Endo, 2017) (Lang, John Peter et al., 2015). For instance, three subunits of the
562 ERMES complex contain a Synaptotagmin-like Mitochondria lipid binding Protein
563 (SMP) domain that forms a hydrophobic lipid transport cavity shared by other
564 proteins of the tubular lipid-binding protein TULIP superfamily (Kopec, Alva et al.,
565 2010, Reinisch & De Camilli, 2016). However, a direct role (independent of its
566 tethering function) of ERMES in lipid transport at ER-mitochondria contact sites is still
567 questioned. In addition, the ERMES complex is not conserved in metazoans. The
568 EMC complex, which has been involved in PS shuttling at ER-mitochondria contact
569 sites in yeast, is instead highly conserved in metazoans (Wideman, 2015). However,
570 no lipid-binding/transfer domain has been found in the EMC proteins, indicating that
571 their implication in lipid transfer at ER-mitochondria contacts is linked to their
572 tethering function rather than to a direct lipid transfer activity. Recently, the
573 mammalian LTP VPS13A has been shown to localize to contact sites including ER-
574 mitochondria contacts. VPS13A contains a lipid-binding domain (VPS13α) that has
575 the ability to harbor multiple phospholipids at once and transfer them between

576 liposomes *in vitro*. However its role in lipid transfer at membrane contact sites *in situ*
577 has not been established yet. Differently from the SMP and VPS13α that can
578 simultaneously host multiple phospholipids, the ORD domain of Osh/ORPs forms a
579 cavity that can host only one lipid at a time (Maeda, Anand et al., 2013, Wang, Ma et
580 al., 2019).

581 ORP5 and ORP8 have recently been shown to counter-exchange PS with PM
582 phosphoinositides PI4P and PIP_2 at ER-PM contact sites in HeLa cells (Chung et al.,
583 2015, Ghai, Du et al., 2017). However PI4P and PIP_2 are not present on the
584 mitochondrial membranes, while PE is highly abundant on these membranes, in
585 addition to being an essential lipid of all biological membranes. Our *in vitro* data show
586 that the ORD domains of ORP5 and ORP8 transport PS, but not other phospholipids
587 such as PE and PC, indicating a specific role of ORP5/8 in PS transport and excluding
588 the possibility that ORP5/8 might also participate in the transport of a fraction of PE
589 back to the ER. It is possible that ORP5/8 cooperate with other LTPs, such as VPS13A,
590 for the exchange of other lipids (including PE) at ER-mitochondria contact sites.
591 Importantly, we have confirmed the role of ORP5/8 in PS transfer by measuring a
592 decrease of PS-derived mitochondrial PE in ORP5 (and even more in ORP5+8)
593 depleted HeLa cells *in situ*. Accordingly, the knockdown of ORP5/8 affects cristae
594 morphology (Fig.1e) and the respiratory function of mitochondria (Galmes et al.,
595 2016), all phenotypes that are expected in the case of decrease in mitochondrial PE
596 (Joshi et al., 2012, Steenbergen et al., 2005). Our data suggest that the gradient of
597 PS at ER-mitochondria contacts is sufficient to trigger the ORP5/8-mediated
598 unidirectional transport of PS from the MAMs, where it is highly enriched, to the
599 mitochondria membranes, where it is rapidly converted into PE and is therefore
600 present at a very low amount. Our findings have important implications in the general

601 field of LTPs, as they suggest that the same LTP can use different means to transfer
602 lipids depending on the local gradients present at the specific membrane contact
603 sites where it is localized. They also suggest a possible new function in PS transport at
604 ER-mitochondria contact sites for the yeast orthologues of ORP5/8, Osh6/7p, whose
605 localization/function at ER-mitochondria contact sites still remain to be addressed
606 (Moser von Filseck, Copic et al., 2015).

607 Another important feature of our work is the observation that ORP5 and ORP8
608 knockdowns do not affect the extent of ER-mitochondria contact sites. These data,
609 consistent with our previous observation that ORP5/8 overexpression does not alter
610 the length of ER-mitochondria contacts (Galmes et al., 2016), confirm that the main
611 function of these proteins at MAMs is lipid transfer and not membrane tethering. This
612 is a unique feature among the LTPs that have been identified so far at MAMs. For
613 instance, modulation of the protein levels of other LTPs such as ERMES in yeast, or
614 VPS13A in mammals, results in an alteration of the extent of ER-mitochondria
615 contact sites (Kornmann, Currie et al., 2009, Kumar, Leonzino et al., 2018). Thus,
616 ORP5/8 represent so far a unique tool to study lipid transport at ER-mitochondria
617 contact sites, independently of membrane tethering.

618 Importantly, our study also reveals that ORP5/8 physically and functionally
619 interact with SAM50 and Mitofilin, two key components of the MIB/MICOS complex
620 that anchor the IMM to the OMM at the level of CJ (Huynen et al., 2016, Ott et al., 2015,
621 Wollweber et al., 2017). The biochemical interaction between ORP5 and
622 SAM50/Mitofilin suggests the existence of a physical link between ER-mitochondria
623 contact sites involved in lipid transport and intra-mitochondria contacts. ORP5
624 localization by IEM at ER-mitochondria contact sites near the CJ, where Mitofilin and
625 MICOS complex also reside, confirms the existence of such tripartite membrane

626 structure. Importantly, we also show that ORP5 cooperates with SAM50 and Mitofilin to
627 facilitate the movement of PS from the ER to the IMM across ER-mitochondria
628 contact sites and the IMS. Taken together these findings provide the first evidence of
629 a physical and functional link between ER-OMM and OMM-IMM contact sites to
630 facilitate transport of PS from the ER to the mitochondria.

631 Finally, we uncover a specific role for ORP5, but not ORP8, in regulating Ca^{2+} import
632 to mitochondria, via a SAM50-VDAC axis. SAM50, in addition to be part of the MIB
633 complex, is also the major subunit of the Sorting and Assembly Machinery (SAM)
634 that mediates membrane insertion and assembly of mitochondrial β-barrel proteins
635 (Hohr et al., 2018, Kozjak et al., 2003). One of the most abundant mitochondria β-
636 barrel proteins is VDAC, which forms a pore that allows the passage of small
637 metabolites and ions such as ATP and Ca^{2+} across the OMM (Colombini, 2012). VDAC
638 exists as three isoforms (VDAC1, 2 and 3) that share common channeling properties.
639 VDAC interacts with the IP3Rs located in the ER membrane via the molecular
640 chaperone GRP75 that links the two proteins together. The interaction between IP3Rs
641 and VDAC acts as a bridge to allow the transfer of Ca^{2+} from the ER to the OMM, and
642 then from the OMM to the mitochondrial matrix through the mitochondrial Ca^{2+} uniporter
643 MCU. Ca^{2+} release from the ER to mitochondria is triggered by IP_3 binding to IP3Rs
644 upon histamine treatment (Rizzuto, Marchi et al., 2009). Here we show that knockdown
645 of ORP5, but not ORP8, increases the protein levels of SAM50 and VDAC as well as the
646 levels of histamine-induced Ca^{2+} import to mitochondria. Importantly, double-knockdown
647 of ORP5 and VDAC rescues the mitochondrial Ca^{2+} increase induced by ORP5
648 silencing, confirming that this increase in Ca^{2+} is indeed VDAC-dependent. Mitochondrial
649 membrane potential has been proposed to influence VDAC open-closed state and
650 consequently import of Ca^{2+} to mitochondria (Tan & Colombini, 2007). However, we did

651 not detect any alteration in mitochondria membrane potential in ORP5 knockdown cells,
652 supporting our idea that the increase in mitochondrial Ca^{2+} observed in ORP5-silenced
653 cells is related to the increase in VDAC protein levels. This is also in accord with
654 previous studies showing that the overexpression of VDAC in HeLa cells enhances
655 mitochondrial Ca^{2+} uptake upon histamine treatment (Rapizzi et al., 2002). Our data
656 also indicate that the effect of VDAC accumulation on mitochondrial Ca^{2+} fluxes does not
657 depend on the modification of ER Ca^{2+} storage or release. Indeed, we observe a similar
658 decrease of ER Ca^{2+} in ORP5 depleted and control cells, upon histamine treatment. Our
659 results correlate well with those of others (Rapizzi et al., 2002) who also observed similar
660 decrease of ER Ca^{2+} in VDAC-overexpressing and control cells.

661 Accumulation of Ca^{2+} in mitochondria, induced by release of Ca^{2+} through IP3R
662 channel, has been recently shown to be involved in cellular senescence in normal
663 cells (Martin & Bernard, 2018, Wiel et al., 2014). Interestingly, we found that
664 knockdown of ORP5, but not ORP8, induces cellular senescence in MCR5 cells.
665 These findings are highly relevant because ORP5 overexpression has been
666 associated to several tumors (Du, Turner et al., 2017). We also show that double-
667 knockdown of ORP5 and SAM50 restores the levels of VDAC protein, as well as of
668 mitochondrial Ca^{2+}, and enables cells to escape from the senescence fate induced by
669 ORP5 depletion. These data confirm that all these phenotypes are dependent on
670 SAM50, and possibly on its known role in the biogenesis of VDAC (Hohr et al., 2018).
671 Future studies are required to further dissect the mechanisms underlying the role of
672 ORP5 in modulating SAM50 protein levels in mitochondria.

673 In conclusion, our data reveal that: 1) ORP5/8 constitute the molecular machinery
674 mediating PS transfer at ER-mitochondria contact sites; 2) ER-mitochondria contacts
675 where ORP5/8 localize are physically and functionally associated with intra-

676 mitochondrial contacts to facilitate the transport of PS from the ER to mitochondria
677 membranes; 3) ORP5 plays a novel specific role in regulating cellular senescence in
678 MCR5 cells by modulating mitochondrial Ca^{2+} fluxes at ER-mitochondria contact sites
679 via SAM50/VDAC (Fig. 8). Our study uncovers a novel link between lipid and Ca^{2+}
680 transport at ER-mitochondria contact sites and provides a first molecular clue on how
681 lipids are transported at ER-mitochondria contact sites. Furthermore, we reveal a
682 specific role of ORP5 in regulating mitochondrial Ca^{2+} homeostasis and cellular
683 senescence in mammalian cells.
684
685
686
687
688
689
690
691
692
693
694
695
696
697
698
699
700

701 **METHODS**

702 **Cell culture, siRNA and transfection**.

703 HeLa cells were cultured in DMEM (Life Technologies) containing GlutaMax (Life
704 Technologies) and supplemented with 10% FBS (Life Technologies) and 1%
705 penicillin/streptomycin (Life Technologies) at 37°C and 5% CO_2. Transfection of
706 plasmids and siRNA oligos (Dharmacon, GE Healthcare) was carried out with
707 lipofectamine 2000 and oligofectamine (Life Technologies) according to
708 manufacturer's instructions.

709 For senescence studies, MRC5 normal human fibroblasts (ATCC) were cultured in
710 Dulbecco′s modified Eagle′s medium (Life Technologies) containing GlutaMax (Life
711 Technologies) and supplemented with 10% FBS (Sigma-Aldrich) and 1%
712 penicillin/streptomycin (Life Technologies). MRC5 were transfected with siRNAs
713 using Dharmafect 1 transfection reagent according to manufacturer's instructions
714 (Dharmacon, GE Healthcare).

715

716 **siRNAs oligonucleotides**

717 For knockdowns, HeLa cells were transfected with siRNA oligos by using
718 oligofectamine (Life Technologies) and cultured for 48 hours prior to analysis.

719 For senescence studies, MRC5 cells were transfected with siRNAs using Dharmafect
720 1 transfection reagent according to manufacturer's instructions (Dharmacon, GE
721 Healthcare).

722 Double-stranded siRNAs were derived from the following references:

siRNA	Company, Reference
OSBPL8	Dharmacon, J-009508-06 (Galmes et al., 2016)
OSBPL8	Dharmacon, J-009508-05 (Galmes et al., 2016)

OSBPL5	Dharmacon, J-009274-10 (Galmes et al., 2016)
OSBPL5	Dharmacon, J-009274-11 (Galmes et al., 2016)
SAMM50	Dharmacon, J-017871-18
SAMM50	Dharmacon, J-017871-19
Non-targeting	Dharmacon, D-001810-10
hVDAC1	5'-AAGCGGGAGCACATTAACCTG-3' (De Stefani, Bononi et al., 2012)
hVDAC2	5'-AAGGATGATCTCAACAAGAGC-3' (De Stefani et al., 2012)
VDAC3	5'-AAGGGTGGCTTGCTGGCTATC-3' (De Stefani et al., 2012)
siMitofilin	5' -AAUUGCUGGAGCUGGCCUUTT-3' (John, Shang et al., 2005)

723

724 **Plasmids and cDNA clones**

725 EGFP-ORP5, EGFP-ORP8, EGFP-ORP5ΔPH, EGFP-ORP8ΔPH, EGFP-
726 ORP5ΔORD and EGFP-ORP5ΔTM were described in (Galmes et al., 2016). The
727 following reagents were kind gifts: 2mt RP ratiometric Pericam from Paolo Pinton
728 (University of Ferrara) (Filippin, Abad et al., 2005); ssHRP-KDEL from T. Schikorski
729 (Schikorski, Young et al., 2007); GST-ORD8 (ORD ORP8, corresponding to aa 328-
730 767) from P. De Camilli (Chung et al., 2015). GECO constructs were from Robert
731 Campbell (Addgene: CMV-R-GECO1 # 32444, CMV-mito-R-GECO1 # 46021, CMV-
732 ER-LAR-GECO1 # 61244, CMV-mito-LAR-GECO1.2 # 61245).

733

734 **Cloning of HA-ORP5, Mitofilin-GFP and GST- ORD5 (ORD ORP5)**

735 cDNAs of ORP5 (full-length), Mitoflin (full-length from FLAG-mitofilin (Ott et al.,
736 2015)) and GST-ORD5 (corresponding to aa 265-703), were amplified by PCR. In all
737 PCR reactions, Herculase II fusion DNA polymerase (Agilent) was used. Primers
738 used were (coding sequence shown in lowercase):

739 5’ AgeI-HA-ORP5_Fw GGCGGC *ACCGGT* cgccacc ATGTACCCATACGATGTTCCA
740 GATTACGCT atgaaggaggaggccttcctc
741 3’ XhoI-STOP-ORP5_Rv GGC *CTCGAG* ctatttgaggatgtggttaatg
742 5’ KpnI-Mitofilin_Fw AGACCCAAGCTT *GGTACC* atg
743 3’ BamHI-GC-Mitofilin_Rv GTAATC *GGATTC* GC ctctggct
744 5’ SalI-TC-ORD5_Fw GCACAG GTCGAC TC gagacccctggggccccggt
745 3’ NotI-STOP-ORD5_Rv GCACA *GCGGCCGC* ctactgtggccggagggctggtcg
746 For the HA-ORP5 cloning the PCR product (carrying the HA tag at the N-terminus of
747 ORP5) was ligated between AgeI and XhoI in the pEGFP-C1 vector (Clontech) and
748 replacing the GFP- with the HA-tag. For the other clonings the PCR products were
749 ligated between KpnI and BamHI for Mitofilin, and between SalI and NotI for ORD5,
750 in the pEGFP-N1 vector (Clontech) to generate Mitofilin-EGFP or in the pGEX-6P-1
751 to generate GST-ORD5.
752
753 **mRNA analyses by quantitative by reverse transcriptase PCR (qPCR)**

754 Total RNA was isolated from HeLa cells transfected with siRNAs for 48 hours as
755 described above, by using a Purelink™ kit (Ambion/Thermo Scientific, Foster City,
756 CA). The RNA (0.5 μg per specimen) was reverse transcribed with a SuperScript
757 VILO™ cDNA synthesis kit (Invitrogen/Thermo Scientific, Carlsbad, CA) according to
758 the manufacturer’s protocol. Quantification of the mRNAs of interest was carried out
759 on a Roche Lightcycler™ 480 II instrument by using SYBR-Green I Master mix
760 (Roche, Basel, Switzerland) and primers specified in Table SX. Succinate
761 dehydrogenase complex. subunit A, the mRNA of which remained markedly stable
762 under the present conditions, was employed as a reference housekeeping mRNA.
763 Relative mRNA levels were calculated by using the –ΔΔCt method.

764 Sequences of the primers used for qPCR:

mRNA	Sequence 5'-3'
SDHA* (housekeeping)	Fw: CATGCTGCCGTGTTCCGTGTGGG
	Rv: GGACAGGGTGTGCTTCCTCCAGTGCTCC
ORP5	Fw: GTGCCGCTGGAGGAGCAGAC
	Rv: AGGGGCTGTGGTCCTCGTATC
SAMM50	Fw: CAAGTGGACCTGATTTTGGAGG
	Rv: AGACGGAGCAATTTTTCACGG
Mitofilin	Fw: GTTGTATCTCAGTATCATGAGCTGG
	Rv: GTTCAGCTGATCAATACGACGA
VDAC1	Fw: ACGTATGCCGATCTTGGCAAA
	Rv: TCAGGCCGTACTCAGTCCATC
VDAC2	Fw: GCTACAGGACTGGGGACTTC
	Rv: AATGCCAAAACGAGTGCAGTT
VDAC3	Fw: GTAAATAATGCCAGCCTGATTG
	Rv: CTTCCAGGGACAAATCTGATG

765 *succinate dehydrogenase complex, subunit A

766

767 For senescence studies, MCR5 cells RNAs were extracted using RNA Extracol lysis
768 buffer (Dutscher). cDNAs were synthesized from total RNA using the Maxima first
769 strand cDNA synthesis kit (Life Technologies). Quantitative PCR mixture contained
770 cDNA, TaqMan mix (Roche), 100 µM of a Universal Probe Library probe (Roche) and
771 200 nM of primers (Sigma-Aldrich) according to manufacturer's instructions. qPCRs
772 were carried out on a FX96 Thermocycler (Bio-Rad). qPCR reactions were as
773 follows: 95°C 10 min, followed with 40 cycles of 95°C 10s, 59°C 30s. The reactions
774 were performed at least in duplicate. The relative amount of mRNA (ORP5, p16, p21,
775 Ki67, PGK1 and HPRT1) was calculated using the comparative Ct (ΔΔCt) method
776 and data were normalized using two housekeeping genes (PGK1 and HPRT1).

777

778 Sequences of the primers and UPL probes used for qPCR:

mRNA/UPL probe	Sequence 5'-3'
CDKN2A (p16) / UPL 34	Fw: GTGGACCTGGCTGAGGAG
	Rv: CTTTCAATCGGGGATGTCTG
p21(CDKN1A) / UPL 32	Fw: TCACTGTCTTGTACCCTTGTGC
	Rv: GGCGTTTGGAGTGGTAGAAAT
Ki67 / UPL 32	Fw: TCAAGGAACTGATTCAGGAGAAG
	Rv: GTGCACTGAAGAACACATTTCC
ORP5 / UPL 17	Fw: GTTGTATCTCAGTATCATGAGCTGG
	Rv: GTTCAGCTGATCAATACGACGA
PGK1 / UPL probe 67	Fw: CAGCTGCTGGGTCTGTCAT
	Rv: GCTGGCTCGGCTTTAACC
HPRT1 / UPL probe 73	Fw: TGACCTTGATTTATTTTGCATACC
	Rv: CGAGCAAGACGTTCAGTCCT

779

780

781 **Antibodies, dyes and reagents list**

782 Primary antibodies used in this study were:

	Antibody	Company & Reference
WB	IP3R-3	BD Transduction Laboratories, 610312
WB	ORP5	SIGMA, HPA038712
WB	ORP5	SIGMA, HPA058727
WB	beta-Actin	Abcam, ab8226
WB	ORP8	GeneTex, GTX121273
IF, WB	SAMM50	SIGMA, HPA034537
WB	Mitofilin	Proteintech, 10179-1-AP
WB	VDAC1	Abcam, ab15895
WB	Cytochrome C	BD Pharmingen, 556433
WB	Total OXPHOS CV-ATP5A	Abcam, ab110413

WB	PDI	GeneTex, GTX30716
WB	VAPB	SIGMA, HPA013144
IF, WB	GFP	Roche, 11814460001
IEM	GFP	Life technologies, A11122
IF	HA	SIGMA, H3663
IF	Cleaved caspase-3	Cell Signaling, 9661
IF	FLAG M2	SIGMA, F1804
IF	MitoTracker® Red CMXRos	M7512, Invitrogen
IF	MitoTracker® Deep Red FM	M22426, Invitrogen

783

784 **Biochemical analyses**

785 ***Western blot***

786 For immunoblotting, cells were resuspended in lysis buffer [50 mM Tris, 150 mM
787 NaCl, 1% Triton X-100, 10 mM EDTA, pH 7.2, and protease inhibitor cocktail
788 (Roche)]. Cell lysates were then centrifuged at 21 000 g for 20 min at 4°C. The
789 supernatants were boiled in reducing SDS sample buffer and proteins were
790 separated using 10% SDS-PAGE and immunoblot was carried using standard
791 methods.

792 For Western blot quantification, bands of protein of interest were detected using
793 ChemiDoc™ Imaging Systems (Life Science Research, Bio-Rad) and analyzed using
794 Image Lab™ Software. All data are presented as mean ±SEM of three experimental
795 replicates.

796 ***Immunoprecipitation of ORPs***

797 HeLa cells transfected with EGFP-tagged ORPs were washed in cold PBS and lysed
798 on ice in lysis buffer [50 mM Tris, 120 mM NaCl, 40 mM Hepes, 0,5% digitonin, 0,5%

799 CHAPS, pH 7.36, and protease inhibitor cocktail (Roche). Cell lysates were then
800 centrifuged at 21 000 g for 20 min at 4°C. Supernatants were then incubated with
801 Chromotek GFP-trap agarose beads (Allele Biotech) for 1 hour at 4°C under rotation.
802 Subsequently beads were washed in 0.1 M phosphate buffer. After extensive washes
803 in cold lysis buffer, immunoprecipitated proteins bound to the beads were processed
804 for Mass Spectrometry analysis (see below) or incubated in sample buffer (containing
805 2% SDS) and then boiled for 1 min. In the latter case immunoprecipitates were
806 loaded and separated in 10% SDS–PAGE gel and immunoblotting was carried out.

807 ***Cell fractionation***

808 HeLa cells ($100x10^6$ cells) were harvested 48 hours after transfection with siRNA
809 oligos and washed with PBS by centrifugation at 600 g for 5 min. The cell pellet was
810 resuspended in starting buffer (225 mM mannitol, 75 mM sucrose and 30 mM Tris-
811 HCl pH 7.4) and homogenized using a Tissue Grinder Dura-Grind®, Stainless Steel,
812 Dounce (Wheaton). The homogenate was centrifuged three times at 600 g for 5 min
813 to remove nuclei and unbroken cells. The crude mitochondria was pelleted by
814 centrifugation at 10 000 g for 10 min. To separate MAM and pure mitochondria
815 fractions, the pellet was resuspended in MRB buffer (250 mM mannitol, 5 mM
816 HEPES and 0.5 mM EGTA, pH 7.4) and layered on top of different concentrations of
817 Percoll gradient (225 mM mannitol, 25 mM HEPES, 1 mM EGTA pH 7.4 and 30% or
818 15% Percoll). After centrifugation at 95 000 g for 30 min, two dense bands containing
819 either the pure mitochondria or MAM fraction were recovered and washed twice with
820 MRB buffer by centrifugation at 6300 g for 10 min to remove residual Percoll and
821 residual contamination. MAM was pelleted by centrifugation at 100 000 g for 1 hour.
822 MAMs and pure mitochondria pellets were resuspended in Lysis Buffer (50 mM Tris,
823 150 mM NaCl, 1% Triton X-100, 10 mM EDTA, pH 7.2, and protease inhibitor

824 cocktail) and protein concentrations were determined by Bradford assay. Equal
825 amount of proteins were loaded on 4-20% gradient SDS-PAGE gels (Biorad) and
826 immunoblotting was carried out. Pure mitochondria were processed for MS-lipidomic
827 analysis (see below).

828 ***Mass spectrometry analysis***

829 Mass Spectrometry (MS) analysis was carried out by the proteomics/mass
830 spectrometry platform in IJM (http://www.ijm.fr/plateformes/spectrometrie-de-masse).
831 Briefly, after washes with binding buffer, immunoprecipitations beads were rinsed
832 with 100 µl of NH4HCO3 25 mmol/l. Proteins on beads were digested overnight at
833 37°C by sequencing grade trypsin (12,5 µg/ml; Promega Madison, Wi, USA) in 20 µl
834 of NH4HCO3 25 mmol/l. Digests were analysed by an Orbitrap Fusion (Thermo
835 Fisher Scientific, San Jose, CA) equipped with a Thermo Scientific EASY-Spray
836 nanoelectrospray ion source and coupled to an Easy nano-LC Proxeon 1000 system
837 (Thermo Fisher Scientific, San Jose, CA). MS/MS data were processed with
838 Proteome Discoverer 1.4 software (Thermo Fisher scientific, San Jose, CA) coupled
839 to an in house Mascot search server (Matrix Science, Boston, MA ; version 2.4.2).
840 MS/MS datas were searched against SwissProt databases with Homo sapiens
841 taxonomy.

842

843 **Mass Spectrometry-lipidomic analysis**

844 700 µl of homogenized cells were mixed with 800 µl 1 N HCl:CH_3OH 1:8 (v/v), 900 µl
845 $CHCl_3$ and 200 µg/ml of the antioxidant 2,6-di-tert-butyl-4-methylphenol (BHT; Sigma
846 Aldrich). The organic fraction was evaporated using a Savant Speedvac spd111v
847 (Thermo Fisher Scientific). Lipid pellets were reconstituted in running solution
848 (CH_3OH:$CHCl_3$:NH_4OH; 90:10:1.25; v/v/v). Phospholipid species were analyzed by

849 electrospray ionization tandem mass spectrometry (ESI-MS/MS) on a hybrid triple
850 quadrupole/linear ion trap mass spectrometer (4000 QTRAP system; Applied
851 Biosystems SCIEX) equipped with a TriVersa NanoMate (Advion Biosciences)
852 robotic nanosource. Phospholipid profiling was executed by (positive or negative)
853 precursor ion or neutral loss scanning at a collision energy of 35 eV for neutral loss
854 141 (phosphatidylethanolamine (PE)). Phospholipid quantification was performed by
855 multiple reaction monitoring (MRM), the transitions being based on the neutral losses
856 or the typical product ions as described above. The MRM dwell time was set to 100
857 ms and typically the signal was averaged over 20 cycles. Lipid standards used were
858 PE25:0 and PE43:6 (Avanti Polar Lipids). The data were corrected for isotope effects
859 as described by (Liebisch, Lieser et al., 2004).
860

861 **Lipid Transfer assay**

862 ***ORP5 and ORP8 ORD domain purification***

863 Escherichia coli BL21DE3 RILP (Invitrogen) cells were transformed with plasmids
864 encoding for GST tagged ORP5 or ORP8 ORD domains following the manufacturer's
865 instruction. Bacteria were then grown overnight at 37°C and used to inoculate a
866 large-scale volume (1L). When the OD_{600} reached 0.4, cultures were cool down and
867 incubate at 18°C until they reached O_{D600} = 0.65. Cells were induced by addition
868 of isopropyl β-D-1-thiogalactopyranoside to a final concentration of 0.1 mM and were
869 incubated overnight at 18°C before harvesting. Cells were resuspended in 35 ml
870 binding buffer (1X PBS, 1 mM EDTA, 1 mM DTT, Protease inhibitor) then 250 units
871 of benzonase nuclease (Sigma) were added to the resuspension. Cells were lysed by
872 sonication and the supernatant was recover after 20 min centrifugation at 184 000g
873 and 4°C. Supernatant containing GST tagged proteins was incubated with 2 ml of

874 Glutathione Sepharose 4 fast flow for 1 hour at 4°C under nutation. Beads were
875 washed using a serie of wash buffer: 1st (1X PBS, 1 mM EDTA, 1 mM DTT), 2nd HSP-
876 removal buffer (50 mM Tris pH7.5, 50 mM KCl, 20 mM MgCl2, 5 mM ATP) then
877 cleavage buffer (50 mM Tris pH 7.5, 150 mM NaCl, 1 mM EDTA, 1 mM DTT).
878 Cleavage of the GST tag was realized overnight at 4°C using Prescission protease.
879 Untagged proteins were eluted with cleavage buffer, flash frozen and stored at -80°C
880 until lipid transfer assay was performed.

881 ***Lipids***

882 1-palmitoyl-2-oleoyl-sn-glycero-3-phosphocholine (POPC), 1,2-dioleoyl-sn-glycero-3-
883 phosphoethanolamine-N-(cap biotinyl) (Biotinyl Cap PE), 1-palmitoyl-2-
884 (dipyrrometheneboron difluoride)undecanoyl-sn-glycero-3-phosphoethanolamine
885 (TopFluor-PE), 1-palmitoyl-2-(dipyrrometheneboron difluoride)undecanoyl-sn-
886 glycero-3-phospho-L-serine (TopFluor-PS), 1-palmitoyl-2-(dipyrrometheneboron
887 difluoride)undecanoyl-sn-glycero-3-phosphocholine (TopFluor-PC) were purchased
888 from Avanti Polar Lipids as chloroform solutions.

889 ***Liposome preparation***

890 1 µmol of the appropriate lipid mixtures in chloroform solution was dried in glass
891 tubes for 10 min under a gentle stream of argon, and then for 1 hour under vacuum.
892 The dried lipid films were resuspended in 1 ml of buffer H (25 mM HEPES/KOH, pH
893 7.7; 150 mM KCL; 10% Glycerol) by vigorously vortexing for 30 min at room
894 temperature. Unilamellar liposomes were produced by seven freeze-thaw cycles (30
895 sec in liquid nitrogen followed by 5 min in a 37°C water bath) and extrusion (at least
896 21 times) through a polycarbonate filter with 100 nm pore size (polycarbonate
897 membranes from Avanti Polar Lipids). The liposomes were then stored on ice.

898 ***Lipid Transfer assay in vitro***

899 The lipid transfer assays were realized with liposomes prepared as described above.
900 The donor liposomes contained 1% mol TopFluor lipids (-PS, -PC or -PE) and 2%
901 mol of Biotinyl Cap PE. The acceptor liposomes contained only POPC. For each
902 reaction, 25 µl of streptavidin-coated magnetic beads (DynabeadsMyOne
903 Streptavidin T1, Invitrogen) were washed in buffer H and mixed with 25 µl of 1 mM
904 donor liposomes. The mixture was incubated for 1 hour at 25°C with intermittent
905 gentle mixing. Bead-bound donor liposomes were then washed, resuspended in 25µl
906 and mixed with 25µl of 1 mM acceptor liposomes and 50µl of buffer H or protein (0.3
907 µM protein and 2.5 µM TopFluor lipids in the reaction solution). The mixture was
908 incubated at 37°C for 1 hour with intermittent gentle mixing. Supernatant containing
909 acceptor liposomes was recovered after binding of bead-bound donor liposomes to a
910 magnetic rack. TopFluor fluorescence of acceptor and donor liposomes was
911 measured (after solubilization with 0.4% (w/v) n-dodecyl-β-D-maltoside) in a
912 SpectraMax M5 plate reader (Molecular Device) equilibrated to 30°C (excitation: 450
913 nm; emission: 510 nm; cutoff: 475 nm; low gain). The percentage of lipids transferred
914 from donor to acceptor liposomes was determined using the following formula:
915 $100*F_{acceptor}/(F_{acceptor}+F_{donor})$.

916

917 **Radiometric assay for the conversion of PS to PE**

918 Hela cells were seeded on 6-well plates and transfected for 48 hours with the non-
919 targeting, ORP5 or ORP8-specific siRNAs specified above by using Oligofectamine
920 (Thermo Fisher Scientific). The cells were then washed and shifted into Hanks
921 balanced salt solution (Gibco) supplemented with a serine-free MEM amino acid
922 mixture and MEM vitamins (Gibco), followed by 4 or 18 hours labeling with 2 µl/well

923 L-[^{3}H(G)]serine (30.9 Ci/mmol, NET24800, Perkin-Elmer). After the labeling, the cells
924 were scraped into 0.9 ml 2% NaCl per well, a 0.1 ml aliquot was withdrawn for
925 protein analysis with the BCA assay (Thermo Fisher Scientific), and, after adding 50
926 nmol of unlabeled PS as carrier, the remaining 0.8 ml was subjected to lipid
927 extraction by an acid modification of the Folch method (Kim, Song et al., 2017). After
928 drying, the lipids were resolved in 50 μl $CHCl_3$ and applied on Merck TLC Silica gel
929 60™ plates, followed by separation by using $CHCl_3$-methanol-acetic acid-H2O
930 (50:30:8:3.5) as solvent. The PS and PE spots identified from the mobility of
931 standards run on the same plates were scraped into scintillation vials for analysis of
932 [^{3}H] radioactivity. The DPM values were corrected for total cell protein, and the ratio
933 of [^{3}H] in PE vs. PS calculated.
934
935 **Fluorescence Microscopy**
936 ***Immunofluorescence and Confocal Microscopy***
937 HeLa cells were seeded on 13 mm glass bottom coverslips (Agar Scientific).
938 Immunofluorescence was carried out one day after transfection. Transfected cells
939 were fixed with 4% PFA/PBS for 15 min at room temperature, washed in PBS and
940 incubated with 50 mM NH4Cl/PBS for 15 min at room temperature. After washing
941 with PBS and blocking buffer (1% BSA/ 0,1% Saponin in PBS), cells were incubated
942 with primary antibodies diluted in blocking buffer for 1 hour at room temperature and
943 then with fluorescently-labeled secondary antibodies. After washing with blocking
944 buffer and then PBS, coverslips were mounted on microscopy slides and images
945 were acquired on Confocal inverted microscope SP8-X (DMI 6000 Leica). Optical
946 sections were acquired with a 63x/1.4 Oil immersion objective using the LAS-X
947 software and fluorescent pictures were collected with a PMTs GaAsP hybride camera

948 (Hamamatsu). Images from a mid-focal plane are shown. Images were processed
949 using Image J.
950
951 **Calcium (Ca^{2+}) indicators**

952 ***Ca^{2+} intake assay using Geco constructs***

953 HeLa cells were seeded on glass bottom ibidi chambers (µ-slide 2 wells) 3 days
954 before imaging. Knockdown of the proteins of interest was realized 2 days before
955 imaging, as described above. The day after knockdown, 0.8 µg of GECO plasmid
956 were transfected with 6 µl of lipofectamine 2000/well (Invitrogen), according to the
957 manufacturer's instructions. The day of imaging, cells were washed 4-5 hours before
958 the imaging with fresh DMEM. Cell imaging was performed on an inverted Nikon Ti
959 Eclipse E microscope coupled with a Spinning Disk (Yokogawa CSU-X1-A1) and
960 cage incubator to control both temperature and CO_2 (37 °C, 5% CO2). After
961 excitation with a 561 nm laser (Coherent, 100 mW), fluorescence from GECO
962 constructs was detected with a 40X oil immersion objective (PLAN FLUOR; NA: 1.30;
963 Nikon) and a Prime 95B sCMOS camera (Photometrics). Images were captured
964 every 5 sec during 10 min. Approximatively 1 min after the start of captures,
965 histamine was added to a final concentration of 100 µM to trigger Ca^{2+} release from
966 intracellular stores. Image analysis was performed using Image J by measuring the
967 fluorescence intensity over time (time-lapse) of cells expressing the GECO
968 constructs. Histograms represent the response of the cell to the addition of histamine
969 shown as the maximum fluorescence (Fmax) after treatment / mean fluorescence
970 before histamine F0.

971 ***Ratiometric Ca^{2+} imaging using a mt-Pericam construct***

HeLa cells were seeded on glass bottom ibidi chambers (µ-slide 2 wells) 3 days before imaging. Knockdown of the proteins of interest was realized 2 days before imaging, as described above. The day after knockdown, 2.4 µg of mt-Pericam plasmid were transfected with 6 µl of lipofectamine 2000/well (Invitrogen), according to the manufacturer's instructions. The day of imaging, cells were washed 4-5 hours before the imaging with fresh DMEM.

Imaging of mt-pericam was performed on an inverted Nikon Ti Eclipse Eclipse-E microscope coupled with a Spinning Disk (Yokogawa, CSU-X1-A1), a 40x CFI Plan Fluor objective (Nikon, NA 1.30, oil immersion) and a sCMOS camera (Photometrics, Prime 95B) with a binning of 2. Knock-down cells expressing pericam constructs were imaged in a controlled atmosphere (37°C, 5% CO_2). For each field of view, a time-lapse was recorded with an image every 8 sec during 10 min. Approximatively 3 min after the start of captures, histamine was added to a final concentration of 100 µM. For each time point mt-pericam fluorescence was collected using a 525/45 bandpass filter (Semrock) after alternative excitation at 405 nm (Vortran, 100mW laser) and 488 nm (Vortran, 150mW laser). A perfect focus system (Nikon) was used to keep the focus constant along the timelapse, the whole system was driven by Metamorph (version 7.7, Molecular Devices).

All the image processing and quantification was performed using a custom script in Image J. First, images were corrected for flat-field and dark noise using reference images respectively acquired on a fluorescent plastic slide (Chroma) and with no light reaching the detector. Regions of interest were also drawn on an empty area of every stack to perform a background subtraction on every image. Then hyperstacks containing two channels were registered to correct any lateral drift of the sample during the acquisition using the Image J plugin "HyperStackReg (v05)" with the

997 “translation” algorithm. Once the stacks were processed, regions of interest were
998 drawn around individual cells, a threshold applied (Mean) and the mean intensity of
999 each cell recorded on each image pair along the time-lapse. For every cell the ratio
1000 488/405 was plotted along the time and only the cells with a stable ratio during the
1001 first 3 min time points and with a sharp increase observed after addition of histamine
1002 were kept for the final analysis.
1003
1004 **Flow cytometry for TMRE analysis**
1005 ***Membrane potential studies using TMRE- Mitochondrial Membrane Potential***
1006 ***Assay Kit***
1007 HeLa cells were seeded on 6-well plates 3 days before TMRE detection and the day
1008 after they were transfected for 48 hours with the non-targeting, ORP5 or ORP8-
1009 specific siRNAs specified above. The day before analysis, the medium was replaced
1010 with DMEM 10% FBS with or without 20 μM CCCP (Carbonyl cyanide m-
1011 chlorophenyl hydrazine) at 37°C and 5% CO_2 to induce mitochondrial depolarization.
1012 After 24 hours, 200 nM of TMRE in DMEM 10% FBS (Mitochondrial Membrane
1013 Potential Assay Kit, abcam ab113852) was added to cells and replaced after 30 min.
1014 Cells were kept at 37°C and 5% CO_2 for additional 15 min and then trypsinized and
1015 resuspended in DMEM (1-2x105 cells in 500 μl). TMRE was then analysed by flow
1016 cytometry.
1017 ***Flow cytometry***
1018 Multicolor flow cytometry was conducted on Beckman Coulter’s CytoFLEX S
1019 cytometer. Analyses were performed using Beckman Coulter’s Kaluza and CytExpert
1020 software. TMRE (Ex/Em = 549/575) was excited by a 561 nm laser and detected

1021 through a 585/542 nm filter channel. All acquisitions were made on 10 000 cells. All
1022 data are presented as mean ±SEM of three independent experimental replicates.
1023

1024 **Apoptosis assay using Cleaved-caspase-3 expression**

1025 HeLa cells were seeded on glass bottom 13 mm coverslips in a 24 well plates. The
1026 next day, 48 hours knockdown of the proteins of interest were realized as described
1027 above. 2 days after the knockdown, cells were treated with 1 µM staurosporine or
1028 with DMSO to induce apoptosis. After 4 hours apoptotic cells were analyzed by
1029 confocal immunofluorescence, using cleaved Caspase-3 antibody and Mitotracker
1030 red to label mitochondria. Cleaved Caspase-3 positive cells were quantified using the
1031 Cell Counter plugin from Image J Software. All data are presented as mean ±SEM of
1032 three experimental replicates.
1033

1034 **Senescence studies using SA-β-Galactosidase assay and crystal violet**
1035 **staining**

1036 For SA-β-galactosidase assay, cells were washed twice with PBS and fixed 5 min
1037 with 2% formaldehyde / 0.2% glutaraldehyde. Cells were then rinsed twice in PBS
1038 and incubated at 37°C overnight in SA-β-Gal staining solution as previously
1039 described (Itahana, Campisi et al., 2007).
1040 For crystal violet staining, cells were washed with PBS, fixed for 15 min in 3.7%
1041 formaldehyde and then stained with 0.5% crystal violet solution. After drying, plates
1042 were scanned.
1043 Relative cell count was determined by dissolving crystal violet in acetic acid solution
1044 and measuring optical density at 595 nM.
1045

1046 **Electron Microscopy Analysis**

1047 ***Conventional EM***

1048 For conventional EM, cells grown on 13 mm glass bottom coverslips (Agar Scientific)
1049 were fixed with 2.5% glutaraldehyde and 2% PFA in 0.1 M cacodylate, 0.05% $CaCl_2$
1050 buffer for 24 hours. After several washes with 0.1 M cacodylate buffer, the cells were
1051 postfixed with 1% OsO_4, 1.5% potassium ferricyanide in 0.1M Cacodylate for 1 hour.
1052 After several washes with 0.1 M cacodylate buffer and H_2O, the cells were stained
1053 with 0.5% uranyl acetate for 24 hours. After several washes with H_2O, the cells were
1054 dehydrated in ethanol and embedded in Epon while on the coverslips. Ultrathin
1055 sections were prepared, counterstained with uranyl acetate and observed under a
1056 MET JEOL 1400 equipped with a Orius High speed (Gatan) camera.

1057 ***HRP Detection***

1058 HeLa cells expressing HRP-KDEL were fixed on coverslips with 1.3% glutaraldehyde
1059 in 0.1 M cacodylate buffer, washed in 0.1 M ammonium phosphate [pH 7.4] buffer for
1060 1 hour and HRP was visualized with 0.5 mg/ml DAB and 0.005% H_2O_2 in 0.1 M
1061 Ammonium Phosphate [pH 7.4] buffer. Development of HRP (DAB dark reaction
1062 product) took between 5 min to 20 min and was stopped by extensive washes with
1063 cold water. Cells were postfixed in 2% OsO_4+1% $K_3Fe(CN)_6$ in 0.1 M cacodylate
1064 buffer at 4°C for 1 hour, washed in cold water and then contrasted in 0.5% uranyl
1065 acetate for 2 hours at 4°C, dehydrated in an ethanol series and embedded in epon as
1066 for conventional EM. Ultrathin sections were counterstained with 2% uranyl acetate
1067 and observed under a FEI Tecnai 12 microscope equipped with a CCD (SiS 1kx1k
1068 keenView) camera.

1069 ***Immunogold labelling***

1070 HeLa cells were fixed with a mixture of 2%PFA and 0.125% glutaraldehyde in 0.1 M
1071 phosphate buffer [pH 7.4] for 2 hours, and processed for ultracryomicrotomy as
1072 described previously (Slot & Geuze, 2007). Ultrathin cryosections were single- or
1073 double-immunogold-labeled with antibodies and protein A coupled to 10 or 15 nm
1074 gold (CMC, UMC Utrecht, The Netherlands), as indicated in the legends to the
1075 figures. Immunogold-labeled cryosections were observed under a FEI Tecnai 12
1076 microscope equipped with a CCD (SiS 1kx1k keenView) camera.

1077 ***Quantifications***

1078 For the quantification of the number of cristae junction in Epon sections, about 200
1079 mitochondria were analyzed in randomly selected cell profiles and cristae junctions
1080 were counted in each of the mitochondria profile and reported as number of
1081 cristae/mitochondria profile. All data are presented as mean ±SEM of three
1082 experimental replicates.

1083 For the quantification of ER-mitochondria contact sites in HRP-stained Epon
1084 sections, the total circumference of each mitochondria and the length of the multiple
1085 HRP-positive ER segments closely associated (<30 nm) with them were measured
1086 by iTEM software (Olympus) on acquired micrographs of HeLa cells for each of 20-
1087 30 cell profiles, as indicated in the figure legends. Cells were randomly selected for
1088 analysis without prior knowledge of transfected plasmid or siRNA. All data are
1089 presented as mean (%) ±SEM of three experimental replicates.

1090 For the quantification of immunogold labeling on ultrathin cryosections, 150 gold
1091 particles were counted on acquired micrographs of randomly selected cell profiles at
1092 specific ranges of distance from CJ (0-50, 50-100, 100-150, 150-200 nm) in each of
1093 three experiments. All data are presented as mean (%) ±SEM of three experimental
1094 replicates.

ACKNOWLEDGEMENTS

We thank Dr V. Kozjak-Pavlovic and P. Pinton for kindly sharing reagents and advices with us. We also thank Dr. R. Legouis for discussion; Claire Boulogne, Mickael Bourge, and Remi Le Borgne for help and consultation with microscopy experiments; Blandine Bourigault, Riikka Kosonen and Liisa Arala for technical assistance. The present work has benefited from Imagerie-Gif core facility supported by l' Agence Nationale de la Recherche (ANR-11-EQPX-0029/Morphoscope, ANR-10-INBS-04/FranceBioImaging; ANR-11-IDEX-0003-02/ Saclay Plant Sciences). For the Immuno-EM and HRP-KDEL EM analysis/quantifications we acknowledge the ImagoSeine core facility of the Institut Jacques Monod, member of IBiSA and the France-BioImaging (ANR-10-INBS-04) infrastructure. We also thank Jean-Michel Camadro and Thibault Leger (IJM proteomics platform) for proteomics analysis. This work was supported by ANR Jeune Chercheur (ANR0015TD and ATIP-Avenir Program to F.G.; the Academy of Finland (grants 285223 and 322647), the Sigrid Juselius Foundation, the Finnish Foundation for Cardiovascular Research and the Magnus Ehrnrooth Foundation to V.M.O.; the Fondation ARC pour la recherche sur le cancer and INCA (N°2018-144) to D.B.; the "Association Française contre les Myopathies" (AFM Research grant 20123) and the ITMO-Inserm Plan Cancer 2014-2019 to D.T.

CONFLICT OF INTEREST

The authors declare that they have no conflict of interest.

1122 **REFERENCES**

1123 Chung J, Torta F, Masai K, Lucast L, Czapla H, Tanner LB, Narayanaswamy P, Wenk MR,
1124 Nakatsu F, De Camilli P (2015) INTRACELLULAR TRANSPORT. PI4P/phosphatidylserine
1125 countertransport at ORP5- and ORP8-mediated ER-plasma membrane contacts. Science
1126 349: 428-32
1127 Colombini M (2012) VDAC structure, selectivity, and dynamics. Biochimica et biophysica
1128 acta 1818: 1457-65
1129 De Stefani D, Bononi A, Romagnoli A, Messina A, De Pinto V, Pinton P, Rizzuto R (2012)
1130 VDAC1 selectively transfers apoptotic Ca2+ signals to mitochondria. Cell Death Differ 19:
1131 267-73
1132 Ding C, Wu Z, Huang L, Wang Y, Xue J, Chen S, Deng Z, Wang L, Song Z, Chen S (2015)
1133 Mitofilin and CHCHD6 physically interact with Sam50 to sustain cristae structure. Sci
1134 Rep 5: 16064
1135 Du X, Turner N, Yang H (2017) The role of oxysterol-binding protein and its related
1136 proteins in cancer. Semin Cell Dev Biol
1137 Du X, Zadoorian A, Lukmantara IE, Qi Y, Brown AJ, Yang H (2018) Oxysterol-binding
1138 protein-related protein 5 (ORP5) promotes cell proliferation by activation of mTORC1
1139 signaling. The Journal of biological chemistry 293: 3806-3818
1140 Filippin L, Abad MC, Gastaldello S, Magalhaes PJ, Sandona D, Pozzan T (2005) Improved
1141 strategies for the delivery of GFP-based Ca2+ sensors into the mitochondrial matrix. Cell
1142 calcium 37: 129-36
1143 Friedman JR, Mourier A, Yamada J, McCaffery JM, Nunnari J (2015) MICOS coordinates
1144 with respiratory complexes and lipids to establish mitochondrial inner membrane
1145 architecture. eLife 4
1146 Galmes R, Houcine A, van Vliet AR, Agostinis P, Jackson CL, Giordano F (2016)
1147 ORP5/ORP8 localize to endoplasmic reticulum-mitochondria contacts and are involved
1148 in mitochondrial function. EMBO reports 17: 800-10
1149 Ghai R, Du X, Wang H, Dong J, Ferguson C, Brown AJ, Parton RG, Wu JW, Yang H (2017)
1150 ORP5 and ORP8 bind phosphatidylinositol-4, 5-biphosphate (PtdIns(4,5)P 2) and
1151 regulate its level at the plasma membrane. Nature communications 8: 757
1152 Giordano F (2018) Non-vesicular lipid trafficking at the endoplasmic reticulum-
1153 mitochondria interface. Biochemical Society transactions 46: 437-452
1154 Guarani V, McNeill EM, Paulo JA, Huttlin EL, Frohlich F, Gygi SP, Van Vactor D, Harper JW
1155 (2015) QIL1 is a novel mitochondrial protein required for MICOS complex stability and
1156 cristae morphology. eLife 4
1157 Harner M, Korner C, Walther D, Mokranjac D, Kaesmacher J, Welsch U, Griffith J, Mann M,
1158 Reggiori F, Neupert W (2011) The mitochondrial contact site complex, a determinant of
1159 mitochondrial architecture. The EMBO journal 30: 4356-70
1160 Herrera-Cruz MS, Simmen T (2017) Of yeast, mice and men: MAMs come in two flavors.
1161 Biol Direct 12: 3
1162 Hohr AIC, Lindau C, Wirth C, Qiu J, Stroud DA, Kutik S, Guiard B, Hunte C, Becker T,
1163 Pfanner N, Wiedemann N (2018) Membrane protein insertion through a mitochondrial
1164 beta-barrel gate. Science 359
1165 Huynen MA, Muhlmeister M, Gotthardt K, Guerrero-Castillo S, Brandt U (2016) Evolution
1166 and structural organization of the mitochondrial contact site (MICOS) complex and the
1167 mitochondrial intermembrane space bridging (MIB) complex. Biochimica et biophysica
1168 acta 1863: 91-101

1169 Itahana K, Campisi J, Dimri GP (2007) Methods to detect biomarkers of cellular
1170 senescence: the senescence-associated beta-galactosidase assay. Methods Mol Biol 371:
1171 21-31
1172 John GB, Shang Y, Li L, Renken C, Mannella CA, Selker JM, Rangell L, Bennett MJ, Zha J
1173 (2005) The mitochondrial inner membrane protein mitofilin controls cristae
1174 morphology. Molecular biology of the cell 16: 1543-54
1175 Joshi AS, Thompson MN, Fei N, Huttemann M, Greenberg ML (2012) Cardiolipin and
1176 mitochondrial phosphatidylethanolamine have overlapping functions in mitochondrial
1177 fusion in Saccharomyces cerevisiae. The Journal of biological chemistry 287: 17589-97
1178 Kim SH, Song HE, Kim SJ, Woo DC, Chang S, Choi WG, Kim MJ, Back SH, Yoo HJ (2017)
1179 Quantitative structural characterization of phosphatidylinositol phosphates from
1180 biological samples. J Lipid Res 58: 469-478
1181 Kopec KO, Alva V, Lupas AN (2010) Homology of SMP domains to the TULIP superfamily
1182 of lipid-binding proteins provides a structural basis for lipid exchange between ER and
1183 mitochondria. Bioinformatics 26: 1927-31
1184 Kornmann B, Currie E, Collins SR, Schuldiner M, Nunnari J, Weissman JS, Walter P (2009)
1185 An ER-mitochondria tethering complex revealed by a synthetic biology screen. Science
1186 325: 477-81
1187 Kozjak V, Wiedemann N, Milenkovic D, Lohaus C, Meyer HE, Guiard B, Meisinger C,
1188 Pfanner N (2003) An essential role of Sam50 in the protein sorting and assembly
1189 machinery of the mitochondrial outer membrane. The Journal of biological chemistry
1190 278: 48520-3
1191 Kozjak-Pavlovic V, Ross K, Benlasfer N, Kimmig S, Karlas A, Rudel T (2007) Conserved
1192 roles of Sam50 and metaxins in VDAC biogenesis. EMBO reports 8: 576-82
1193 Kumar N, Leonzino M, Hancock-Cerutti W, Horenkamp FA, Li P, Lees JA, Wheeler H,
1194 Reinisch KM, De Camilli P (2018) VPS13A and VPS13C are lipid transport proteins
1195 differentially localized at ER contact sites. The Journal of cell biology 217: 3625-3639
1196 Lang A, John Peter AT, Kornmann B (2015) ER-mitochondria contact sites in yeast:
1197 beyond the myths of ERMES. Current opinion in cell biology 35: 7-12
1198 Liebisch G, Lieser B, Rathenberg J, Drobnik W, Schmitz G (2004) High-throughput
1199 quantification of phosphatidylcholine and sphingomyelin by electrospray ionization
1200 tandem mass spectrometry coupled with isotope correction algorithm. Biochimica et
1201 biophysica acta 1686: 108-17
1202 Ma X, Warnier M, Raynard C, Ferrand M, Kirsh O, Defossez PA, Martin N, Bernard D
1203 (2018) The nuclear receptor RXRA controls cellular senescence by regulating calcium
1204 signaling. Aging Cell 17: e12831
1205 Maeda K, Anand K, Chiapparino A, Kumar A, Poletto M, Kaksonen M, Gavin AC (2013)
1206 Interactome map uncovers phosphatidylserine transport by oxysterol-binding proteins.
1207 Nature 501: 257-61
1208 Martin N, Bernard D (2018) Calcium signaling and cellular senescence. Cell calcium 70:
1209 16-23
1210 Moser von Filseck J, Copic A, Delfosse V, Vanni S, Jackson CL, Bourguet W, Drin G (2015)
1211 INTRACELLULAR TRANSPORT. Phosphatidylserine transport by ORP/Osh proteins is
1212 driven by phosphatidylinositol 4-phosphate. Science 349: 432-6
1213 Nagai T, Sawano A, Park ES, Miyawaki A (2001) Circularly permuted green fluorescent
1214 proteins engineered to sense Ca2+. Proceedings of the National Academy of Sciences of
1215 the United States of America 98: 3197-202

1216 Ott C, Dorsch E, Fraunholz M, Straub S, Kozjak-Pavlovic V (2015) Detailed analysis of the
1217 human mitochondrial contact site complex indicate a hierarchy of subunits. PloS one 10:
1218 e0120213
1219 Patron M, Raffaello A, Granatiero V, Tosatto A, Merli G, De Stefani D, Wright L,
1220 Pallafacchina G, Terrin A, Mammucari C, Rizzuto R (2013) The mitochondrial calcium
1221 uniporter (MCU): molecular identity and physiological roles. The Journal of biological
1222 chemistry 288: 10750-8
1223 Pulli I, Lassila T, Pan G, Yan D, Olkkonen VM, Tornquist K (2018) Oxysterol-binding
1224 protein related-proteins (ORPs) 5 and 8 regulate calcium signaling at specific cell
1225 compartments. Cell calcium 72: 62-69
1226 Rapizzi E, Pinton P, Szabadkai G, Wieckowski MR, Vandecasteele G, Baird G, Tuft RA,
1227 Fogarty KE, Rizzuto R (2002) Recombinant expression of the voltage-dependent anion
1228 channel enhances the transfer of Ca2+ microdomains to mitochondria. The Journal of
1229 cell biology 159: 613-24
1230 Reinisch KM, De Camilli P (2016) SMP-domain proteins at membrane contact sites:
1231 Structure and function. Biochimica et biophysica acta 1861: 924-927
1232 Rizzuto R, Marchi S, Bonora M, Aguiari P, Bononi A, De Stefani D, Giorgi C, Leo S, Rimessi
1233 A, Siviero R, Zecchini E, Pinton P (2009) Ca(2+) transfer from the ER to mitochondria:
1234 when, how and why. Biochimica et biophysica acta 1787: 1342-51
1235 Schikorski T, Young SM, Jr., Hu Y (2007) Horseradish peroxidase cDNA as a marker for
1236 electron microscopy in neurons. Journal of neuroscience methods 165: 210-5
1237 Scorrano L, De Matteis MA, Emr S, Giordano F, Hajnoczky G, Kornmann B, Lackner LL,
1238 Levine TP, Pellegrini L, Reinisch K, Rizzuto R, Simmen T, Stenmark H, Ungermann C,
1239 Schuldiner M (2019) Coming together to define membrane contact sites. Nature
1240 communications 10: 1287
1241 Shiao YJ, Lupo G, Vance JE (1995) Evidence that phosphatidylserine is imported into
1242 mitochondria via a mitochondria-associated membrane and that the majority of
1243 mitochondrial phosphatidylethanolamine is derived from decarboxylation of
1244 phosphatidylserine. The Journal of biological chemistry 270: 11190-8
1245 Slot JW, Geuze HJ (2007) Cryosectioning and immunolabeling. Nature protocols 2: 2480-
1246 91
1247 Steenbergen R, Nanowski TS, Beigneux A, Kulinski A, Young SG, Vance JE (2005)
1248 Disruption of the phosphatidylserine decarboxylase gene in mice causes embryonic
1249 lethality and mitochondrial defects. The Journal of biological chemistry 280: 40032-40
1250 Tamura Y, Endo T (2017) Role of Intra- and Inter-mitochondrial Membrane Contact
1251 Sites in Yeast Phospholipid Biogenesis. Advances in experimental medicine and biology
1252 997: 121-133
1253 Tan W, Colombini M (2007) VDAC closure increases calcium ion flux. Biochimica et
1254 biophysica acta 1768: 2510-5
1255 Tatsuta T, Scharwey M, Langer T (2014) Mitochondrial lipid trafficking. Trends in cell
1256 biology 24: 44-52
1257 Vance JE (1990) Phospholipid synthesis in a membrane fraction associated with
1258 mitochondria. The Journal of biological chemistry 265: 7248-56
1259 Vance JE (2014) MAM (mitochondria-associated membranes) in mammalian cells: lipids
1260 and beyond. Biochimica et biophysica acta 1841: 595-609
1261 Vance JE, Tasseva G (2013) Formation and function of phosphatidylserine and
1262 phosphatidylethanolamine in mammalian cells. Biochimica et biophysica acta 1831:
1263 543-54

Wang H, Ma Q, Qi Y, Dong J, Du X, Rae J, Wang J, Wu WF, Brown AJ, Parton RG, Wu JW, Yang H (2019) ORP2 Delivers Cholesterol to the Plasma Membrane in Exchange for Phosphatidylinositol 4, 5-Bisphosphate (PI(4,5)P2). Mol Cell 73: 458-473 e7

Wideman JG (2015) The ubiquitous and ancient ER membrane protein complex (EMC): tether or not? F1000Res 4: 624

Wiel C, Lallet-Daher H, Gitenay D, Gras B, Le Calve B, Augert A, Ferrand M, Prevarskaya N, Simonnet H, Vindrieux D, Bernard D (2014) Endoplasmic reticulum calcium release through ITPR2 channels leads to mitochondrial calcium accumulation and senescence. Nature communications 5: 3792

Wollweber F, von der Malsburg K, van der Laan M (2017) Mitochondrial contact site and cristae organizing system: A central player in membrane shaping and crosstalk. Biochimica et biophysica acta 1864: 1481-1489

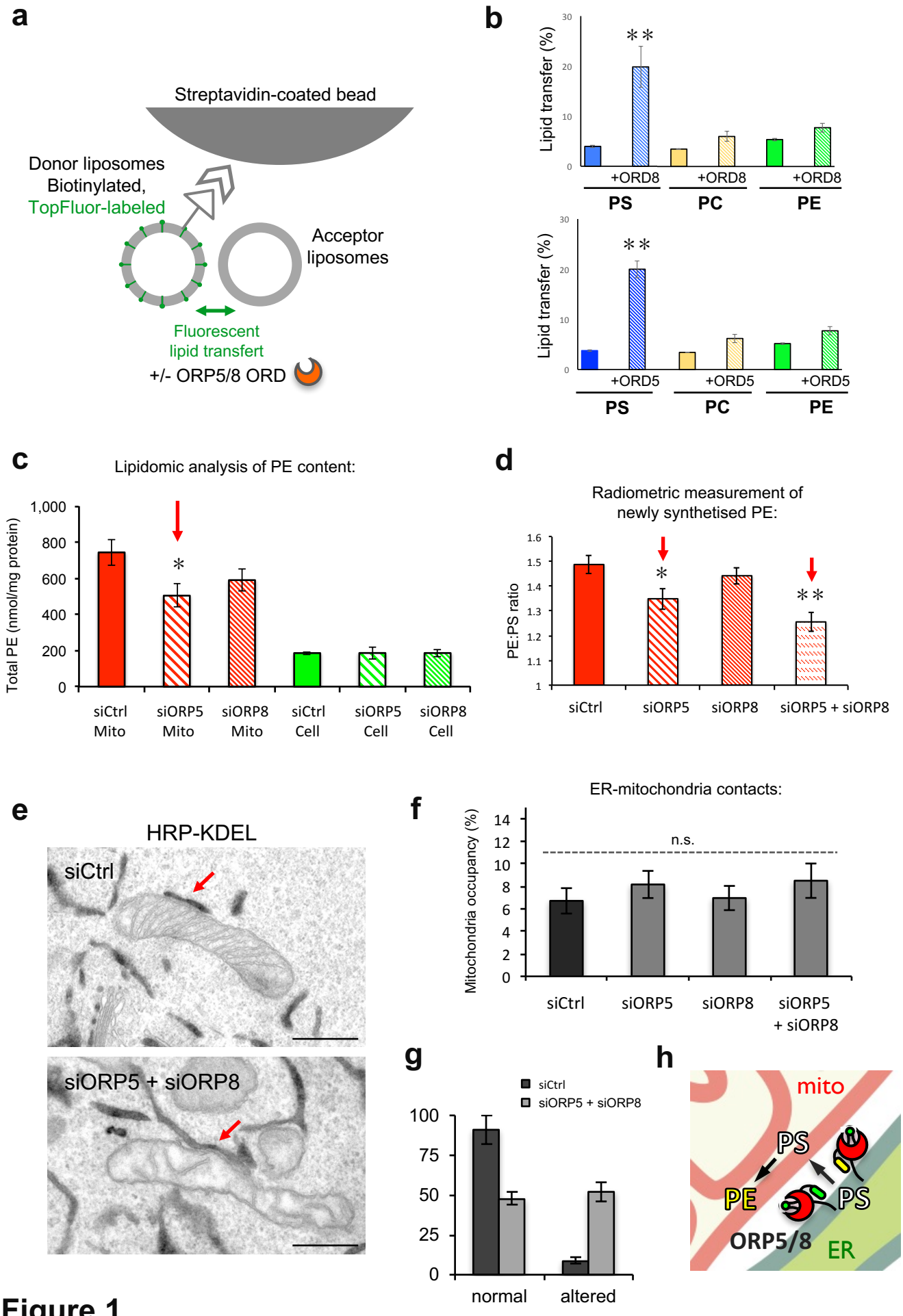
a
Streptavidin-coated bead
Donor liposomes
Biotinylated,
TopFluor-labeled
Acceptor
liposomes
Fluorescent
lipid transfert
+/- ORP5/8 ORD
b
Lipid transfer (%)
+ORD8
+ORD8
+ORD8
PS
PC
PE
Lipid transfer (%)
+ORD5
+ORD5
+ORD5
PS
PC
PE
c
Lipidomic analysis of PE content:
Total PE (nmol/mg protein)
siCtrl Mito
siORP5 Mito
siORP8 Mito
siCtrl Cell
siORP5 Cell
siORP8 Cell
d
Radiometric measurement of
newly synthetised PE:
PE:PS ratio
siCtrl
siORP5
siORP8
siORP5 + siORP8
e
HRP-KDEL
siCtrl
siORP5 + siORP8
f
ER-mitochondria contacts:
Mitochondria occupancy (%)
n.s.
siCtrl
siORP5
siORP8
siORP5
+ siORP8
g
siCtrl
siORP5 + siORP8
normal
altered
h
mito
PS
PE
PS
ORP5/8
ER

Figure 1

Figure 1. ORP5 and ORP8 mediate PS transfer *in vitro* and at ER-mitochondria contact sites

(a) Schematic cartoon showing the *in vitro* assay used to study ORP5/8 ORD-mediated lipid transport between liposomes. (b) Donor liposomes containing fluorescent lipids (97 mol% POPC, 1 mol% TopFluor-PS, -PC or -PE and 2 mol% of biotinylated-PE) and pre-bound to streptavidin beads were mixed at a 1:1 molar ratio with acceptor liposomes (100 mol% POPC) in the presence or absence of ORP5 or ORP8 ORD domains (250 μM of donor and acceptor liposomes and 0,3 μM of proteins in the reaction solution). The increase in fluorescence in the acceptor liposomes, which remain unbound in the solution, was measured after 1 hour of incubation at 37° C. Data are presented as % of transferred lipid ±SEM and are the mean of six independent replicates. **P<0,001 (c) Mass spectrometry (MS)-based quantification of the PE content (nmol/mg protein) of mitochondria isolated from Ctrl, ORP5 or ORP8 knockdown cells and of Ctrl, ORP5 or ORP8 knockdown intact cells. Data are shown as mean of three independent replicates ±SEM. *P<0,05. (d) Ctrl, ORP5, ORP8 or ORP5+ORP8 double-knockdown cells were incubated with L-[^{3}H(G)]serine (30.9 Ci/mmol) for 18 hour. After extraction and separation of lipids by TLC, PS and PE spots were scraped and analysed for [^{3}H] radioactivity, as described under “Methods”. Each condition was analyzed in triplicate in each of three independent biological replicates. Data are presented as mean of PE:PS ratio ±SEM. *P<0,05, **P<0,01 compared to Ctrl. (e) Electron micrographs of HRP-KDEL-expressing HeLa cells treated with Ctrl siRNAs or siRNAs against ORP5 and ORP8 (siORP5+siORP8). Red arrows indicate ER-mitochondria contact sites. Scale bar, 500 nm. (f) Quantifications of the extent of ER-mitochondria contact sites in Ctrl, ORP5, ORP8 and ORP5+ORP8 knockdown cells expressing HRP-KDEL. Data are shown as % of the ER in contact with mitochondria (mitochondria occupancy) ±SEM, n = 20 cell profiles and ±900 mitochondria; n.s; not significant. (g) Quantifications of the number of mitochondria with aberrant cristae morphology in the indicated siRNA conditions. Data are shown as % of mitochondria ±SEM, n = 20 cell profiles and ±700 mitochondria. **P<0,01 compared to siCtrl. (h) Schematic representation of non-vesicular PS transfer mediated by ORP5/8 at ER-mitochondria contact sites. PS is transported to mitochondrial membranes where it is rapidly converted into mitochondrial PE.

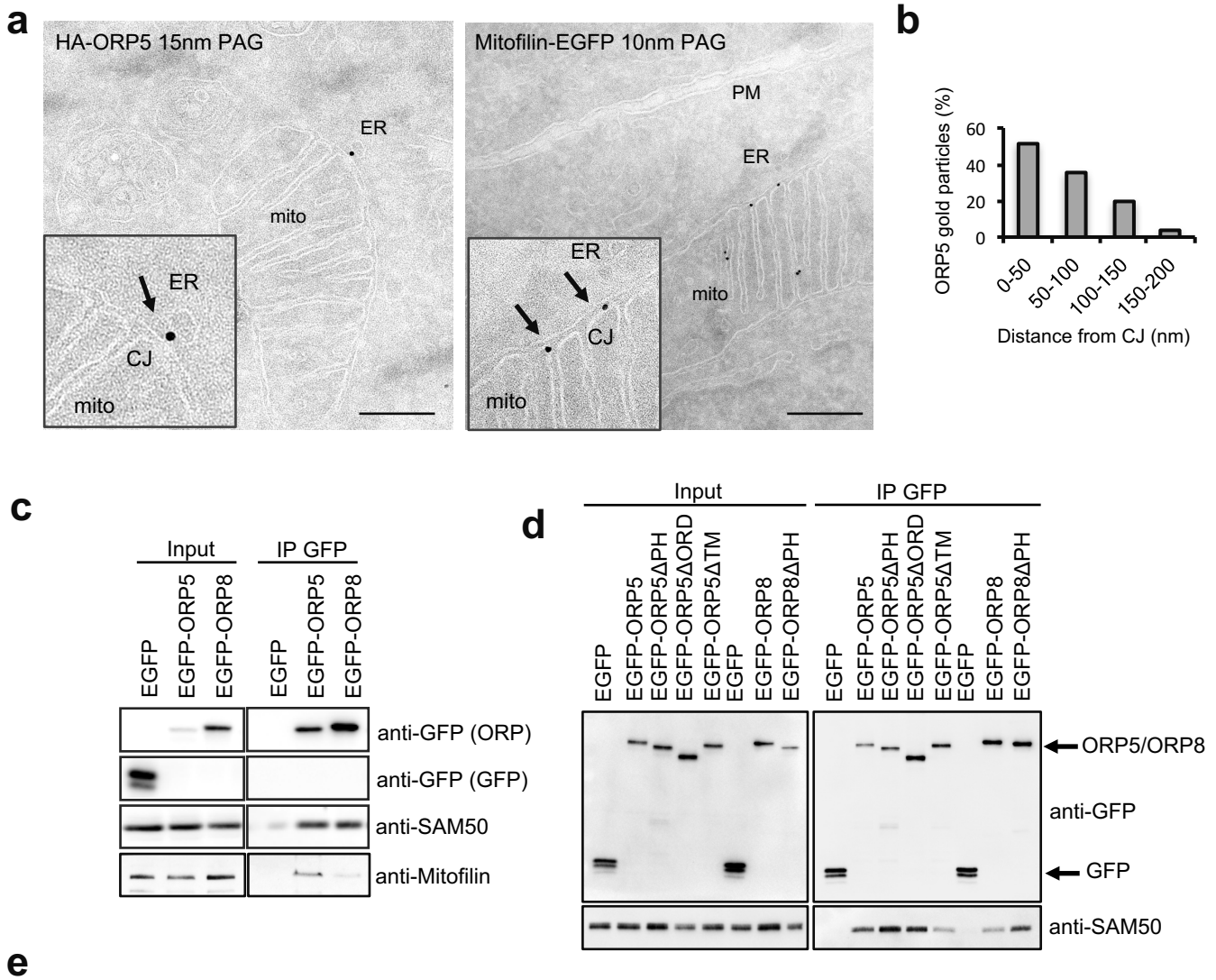
a
HA-ORP5 15nm PAG
ER
mito
ER
CJ
mito
Mitofilin-EGFP 10nm PAG
PM
ER
mito
ER
CJ
mito
b
ORP5 gold particles (%)
60
40
20
0
0-50
50-100
100-150
150-200
Distance from CJ (nm)
c
Input
IP GFP
EGFP
EGFP-ORP5
EGFP-ORP8
anti-GFP (ORP)
anti-GFP (GFP)
anti-SAM50
anti-Mitofilin
d
Input
IP GFP
EGFP
EGFP-ORP5
EGFP-ORP5ΔPH
EGFP-ORP5ΔORD
EGFP-ORP5ΔTM
EGFP
EGFP-ORP8
EGFP-ORP8ΔPH
ORP5/ORP8
anti-GFP
GFP
anti-SAM50

e

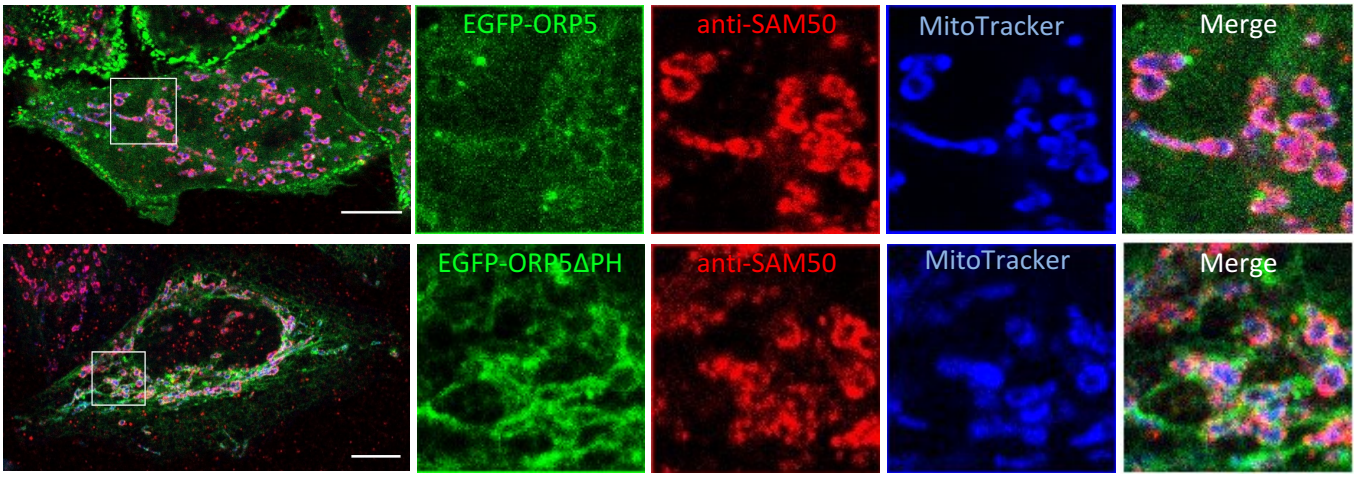
EGFP-ORP5
anti-SAM50
MitoTracker
Merge
EGFP-ORP5ΔPH
anti-SAM50
MitoTracker
Merge

Figure 2

Figure 2. ORP5 and ORP8 interact with the MIB/MICOS complex at ER-mitochondria contacts near CJ

(a) Electron micrograph of ultrathin cryosection of HeLa cells transfected with HA-ORP5 or Mitofilin-EGFP and immunogold stained with anti-HA or anti-GFP (10 or 15 nm gold) showing HA-ORP5 localization at ER-mitochondria contacts in close proximity to CJ (arrow) and the localization of the MICOS complex (Mitofilin) at CJ (arrows). Scale bar 150 nm. (b) Quantification of the proximity of HA-ORP5 gold particles to the CJ. Results are presented as the percentage of ORP5 gold particles (n = 23 cell profiles) at specific ranges of distance from CJ (0-50, 50-100, 100-150, 150-200 nm). (c) EGFP-ORP5, EGFP-ORP8 or EGFP alone were transfected in HeLa cells then immuno-precipitated from lysates and analyzed by western blot using antibodies against GFP (for ORP5 or ORP8), Mitofilin or SAM50. (d) EGFP-ORP5, EGFP-ORP5ΔPH, EGFP-ORP5ΔORD, EGFP-ORP5ΔTM, EGFP-ORP8, EGFP-ORP8ΔPH or EGFP alone were transfected in HeLa cells then immuno-precipitated from lysates and analyzed by western blot using antibodies against GFP (for ORP5 or ORP8) or against SAM50. (e) Fluorescent images of HeLa cells transfected with either EGFP-ORP5 or EGFP-ORP5ΔPH and stained with MitoTracker and anti-SAM50 antibody. Insets show magnifications of the boxed regions. Scale bar, 10 μm.

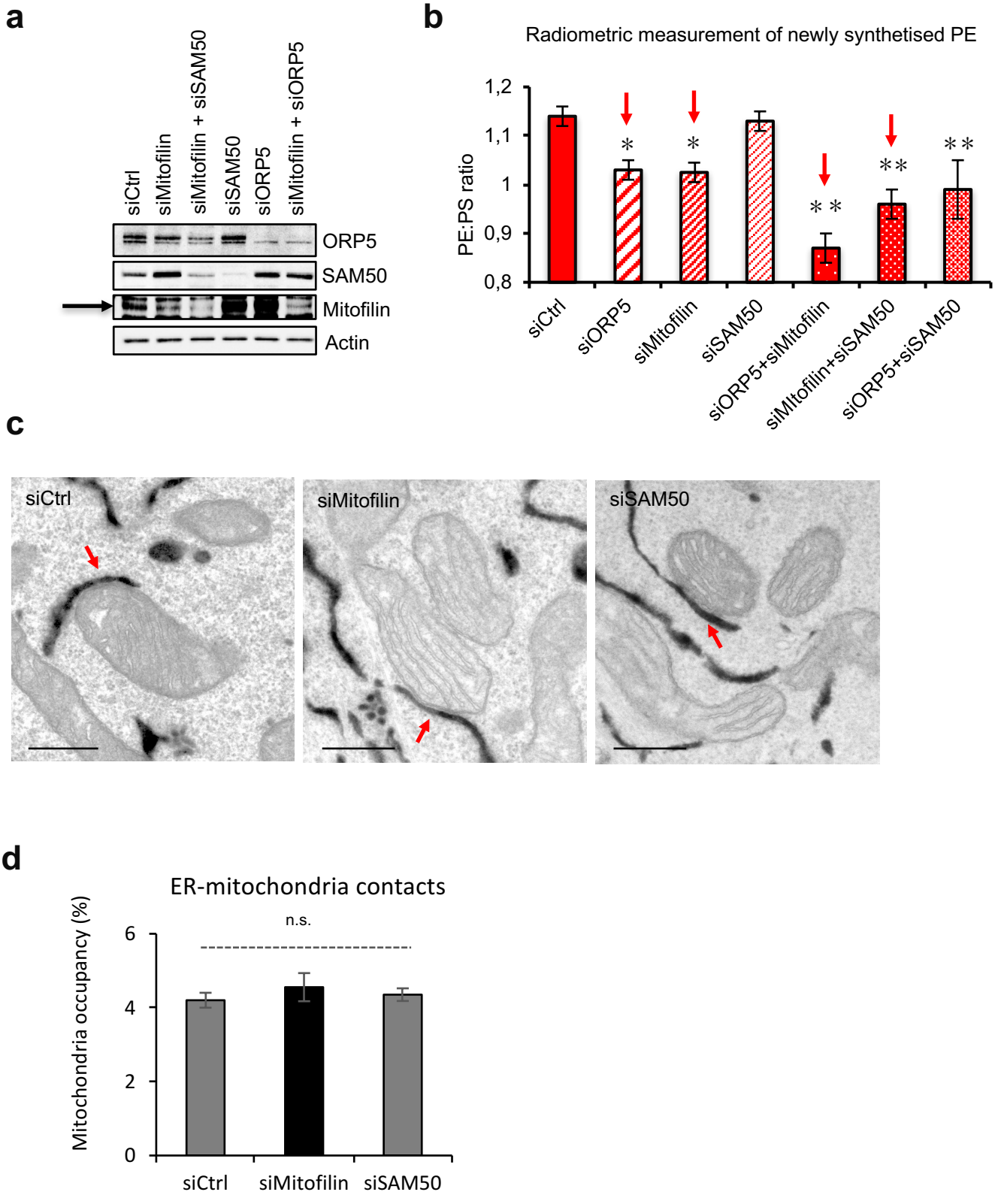
a
siCtrl
siMitofilin
siMitofilin + siSAM50
siSAM50
siORP5
siMitofilin + siORP5
ORP5
SAM50
Mitofilin
Actin
b
Radiometric measurement of newly synthetised PE
PE:PS ratio
1,2
1,1
1
0,9
0,8
siCtrl
siORP5
siMitofilin
siSAM50
siORP5+siMitofilin
siMltofilin+siSAM50
siORP5+siSAM50
c
siCtrl
siMitofilin
siSAM50
d
ER-mitochondria contacts
n.s.
Mitochondria occupancy (%)
6
4
2
0
siCtrl
siMitofilin
siSAM50

Figure 3

Figure 3. ORP5 and the MIB/MICOS complex function together to mediate non-vesicular transport of PS from the ER to mitochondrial membranes

(a) Western analysis showing ORP5, SAM50, Mitofilin and Actin levels in protein lysates from HeLa cells treated with siRNA against Ctrl, ORP5, Mitofilin or SAM50. Arrow indicates the specific band for Mitofilin. (b) Radiometric measurement of PS-to-PE conversion in the indicated siRNAs. Data are presented as mean of PE:PS ratio ±SEM. Each condition was performed in triplicate in each of the independent biological replicates (n = 5 for siCtrl and siORP5; n = 4 for siSAM50; n = 3 for the other siRNAs conditions). *P<0,05, **P<0,01 compared to Ctrl. (c) Representative electron micrographs of HeLa cells treated with Ctrl siRNAs or siRNAs against Mitofilin or SAM50 and transfected with HRP-KDEL. Red arrows indicate ER-mitochondria contact sites. Scale bar, 500 nm. (d) Quantifications of the extent of ER-mitochondria contact sites in Ctrl, Mitofilin and SAM50 knockdown cells expressing HRP-KDEL. Data are shown as % of the ER in contact with mitochondria (mitochondria occupancy) ±SEM, n = 30 for siCtrl, n = 20 cell profiles for siMitofilin and siSAM50 and 1 000 mitochondria; n.s; not significant.

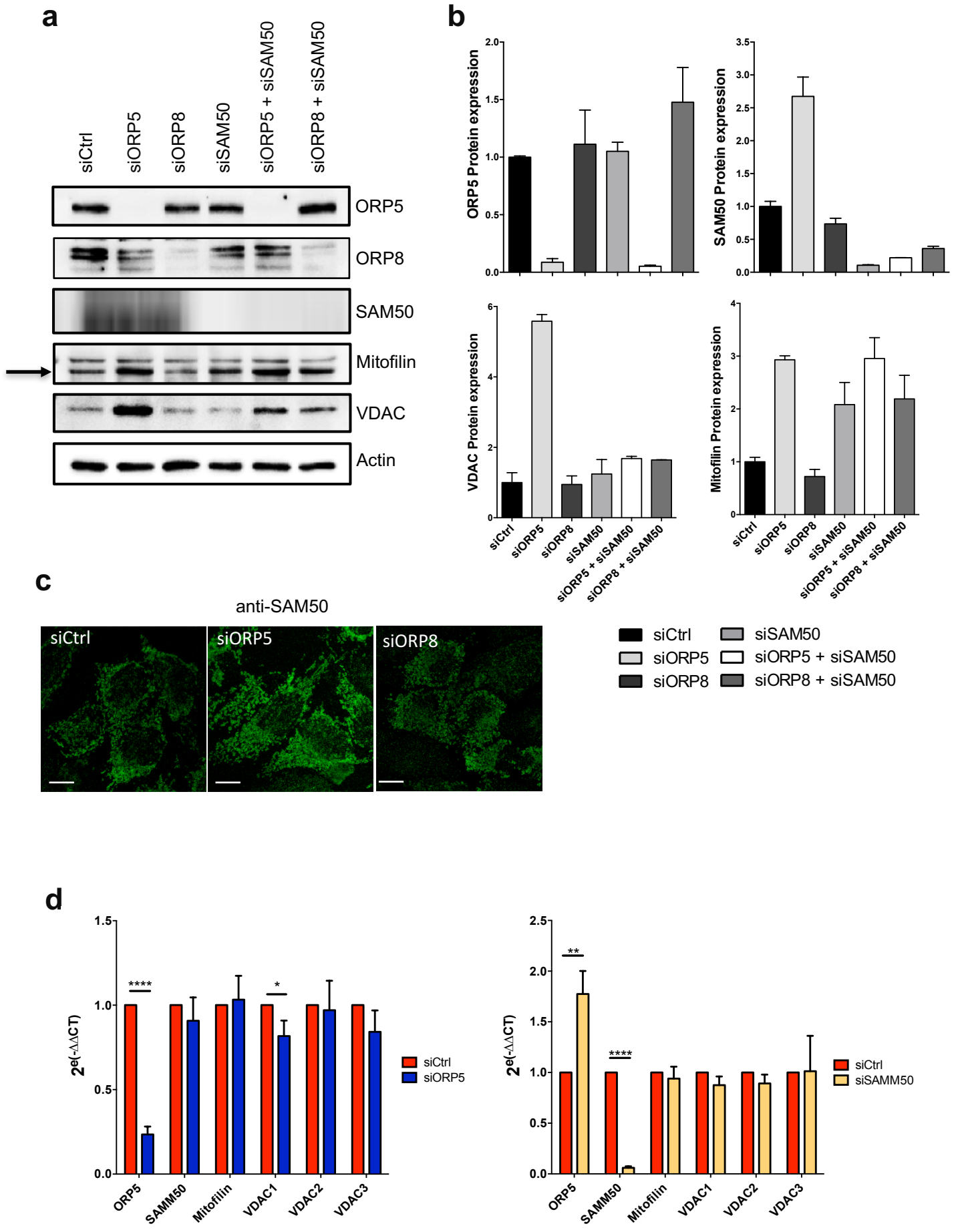
a
siCtrl
siORP5
siORP8
siSAM50
siORP5 + siSAM50
siORP8 + siSAM50
ORP5
ORP8
SAM50
Mitofilin
VDAC
Actin
b
ORP5 Protein expression
SAM50 Protein expression
VDAC Protein expression
Mitofilin Protein expression
siCtrl
siORP5
siORP8
siSAM50
siORP5 + siSAM50
siORP8 + siSAM50
c
anti-SAM50
siCtrl
siORP5
siORP8
siCtrl
siORP5
siORP8
siSAM50
siORP5 + siSAM50
siORP8 + siSAM50
d
2e(-ΔΔCT)
****
*
siCtrl
siORP5
ORP5
SAMM50
Mitofilin
VDAC1
VDAC2
VDAC3
**
****
siCtrl
siSAMM50

Figure 4

Figure 4. Silencing of ORP5 but not ORP8 specifically increases VDAC protein level in a SAM50-dependent manner

(a) Western analysis showing ORP5, ORP8, SAM50, Mitofilin, VDAC and Actin levels in protein lysates from HeLa cells treated with either Ctrl siRNAs, or with siRNAs against ORP5, ORP8, or SAM50. (b) Quantification of ORP5, SAM50, VDAC and Mitofilin protein expression in the indicated knockdown conditions. Normalized data are shown as mean ±SEM (n = 3). (c) Confocal images of Ctrl, ORP5 and ORP8 knockdown HeLa cells immunostained using anti-SAM50 antibody. Scale bar, 10 μm. (d) Quantitative RT-PCR analysis of ORP5, SAM50, Mitofilin, VDAC1, VDAC2 and VDAC3 in ORP5 (left graph) or in SAM50 (right graph) knockdown cells versus control HeLa cells. y axis: $2^{(-\Delta\Delta Ct)}$ value represents differences between the mean Ct (Cycle threshold) values of tested genes and those of reference gene (SDHA).

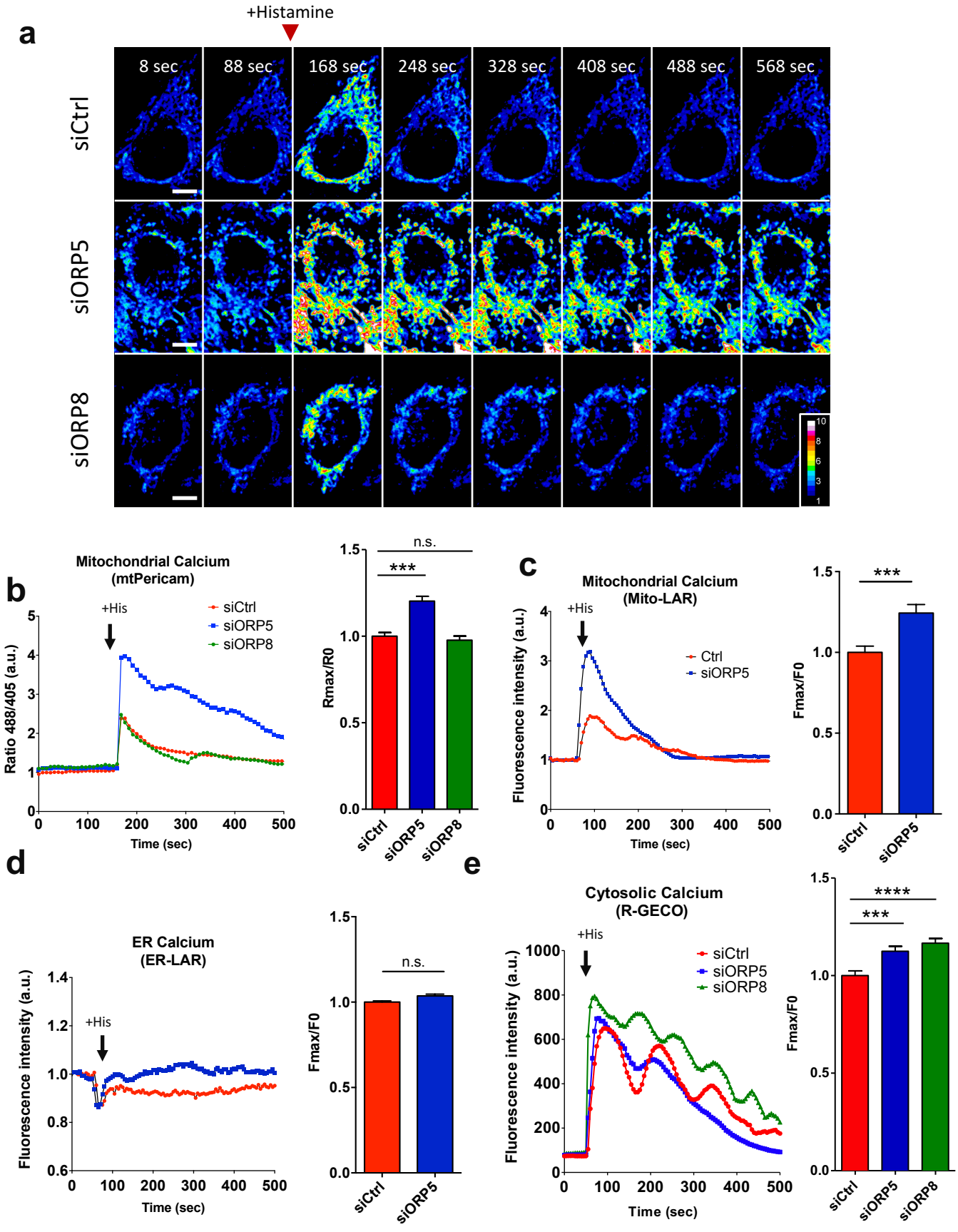
a
+Histamine
8 sec
88 sec
168 sec
248 sec
328 sec
408 sec
488 sec
568 sec
siCtrl
siORP5
siORP8
b
Mitochondrial Calcium
(mtPericam)
+His
siCtrl
siORP5
siORP8
Ratio 488/405 (a.u.)
Time (sec)
Rmax/R0
n.s.
***
c
Mitochondrial Calcium
(Mito-LAR)
Ctrl
siORP5
Fluorescence intensity (a.u.)
Fmax/F0
d
ER Calcium
(ER-LAR)
e
Cytosolic Calcium
(R-GECO)
****

Figure 5

Figure 5. Silencing of ORP5 but not ORP8 increases mitochondrial calcium

(a) Pseudocolor 488/405 ratio time-lapse images of a representative Ctrl, ORP5 or ORP8 knockdown HeLa cell expressing mt-Pericam before and after histamine treatment. Scale bar 10 μm. (b) Representative curves of Ctrl, ORP5 and ORP8 knockdown HeLa cells expressing mt-Pericam showing the ratio of Pericam fluorescence before and after histamine treatment (+His). The change in the ratio of Pericam fluorescence after histamine treatment under each condition was compared (Rmax/R0). Data are presented as normalized mean ±SEM, n = 3 per condition, ***, p< 0.001; n.s; not significant. (c) Representative curves of Ctrl and ORP5 knockdown HeLa cells expressing the GECO construct Mito-LAR showing the fluorescence before and after histamine treatment. The change in fluorescence after histamine treatment under each condition was compared (Fmax/F0). Data are presented as normalized mean ±SEM, n = 3 per condition, ***, p< 0.001; n.s; not significant. (d) Representative curves of Ctrl and ORP5 knockdown HeLa cells expressing the GECO construct ER-LAR showing the fluorescence before and after histamine treatment. The change in fluorescence after histamine treatment under each condition was compared (Fmax/F0). Data are presented as normalized mean ±SEM, n = 3 per condition, n.s; not significant. (e) Representative curves of Ctrl, ORP5 and ORP8 knockdown HeLa cells expressing the GECO construct R-GECO showing the fluorescence before and after histamine treatment. The change in fluorescence after histamine treatment under each condition was compared (Fmax/F0). Data are presented as normalized mean ±SEM, n = 3 per condition, ***, p< 0.001 and ****, p< 0.0001; n.s; not significant.

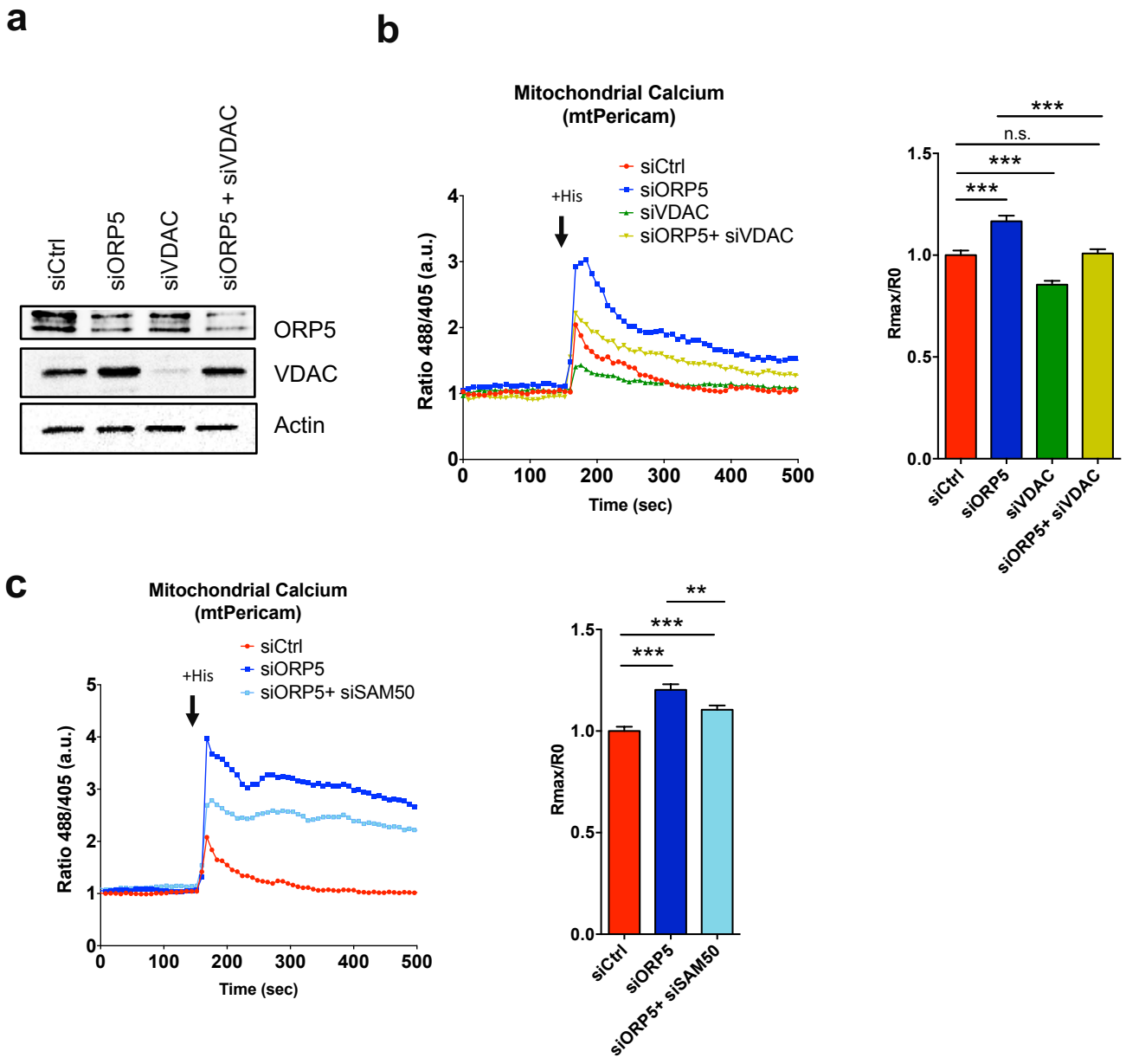
a
siCtrl
siORP5
siVDAC
siORP5 + siVDAC
ORP5
VDAC
Actin
b
Mitochondrial Calcium
(mtPericam)
+His
siCtrl
siORP5
siVDAC
siORP5+ siVDAC
Ratio 488/405 (a.u.)
Time (sec)
0
100
200
300
400
500
1
2
3
4
***
n.s.
***
***
1.5
1.0
0.5
0.0
Rmax/R0
siCtrl
siORP5
siVDAC
siORP5+ siVDAC
c
Mitochondrial Calcium
(mtPericam)
+His
siCtrl
siORP5
siORP5+ siSAM50
Ratio 488/405 (a.u.)
Time (sec)
5
**
***
***
Rmax/R0
siCtrl
siORP5
siORP5+ siSAM50

Figure 6

Figure 6. Calcium increase induced by ORP5 knockdown is dependent on VDAC

(a) Western analysis showing ORP5 and VDAC protein levels in Ctrl, ORP5 and VDAC siRNA-treated HeLa cells. (b). Representative curves of Ctrl, ORP5, VDAC and ORP5+VDAC knockdown HeLa cells expressing mt-Pericam showing the ratio of Pericam fluorescence before and after histamine treatment (+His). The change in the ratio of Pericam fluorescence after histamine treatment under each condition was compared (Rmax/R0). Data are presented as normalized mean ±SEM, n = 3 per condition, ***, $p < 0.001$; n.s; not significant. (c). Representative curves of Ctrl, ORP5 and ORP5+SAM50 knockdown HeLa cells expressing mt-Pericam showing the ratio of Pericam fluorescence before and after histamine treatment (+His). The change in the ratio of Pericam fluorescence after histamine treatment under each condition was compared (Rmax/R0). Data are presented as normalized mean ±SEM, n = 3 per condition, ***, $p < 0.001$; n.s; not significant.

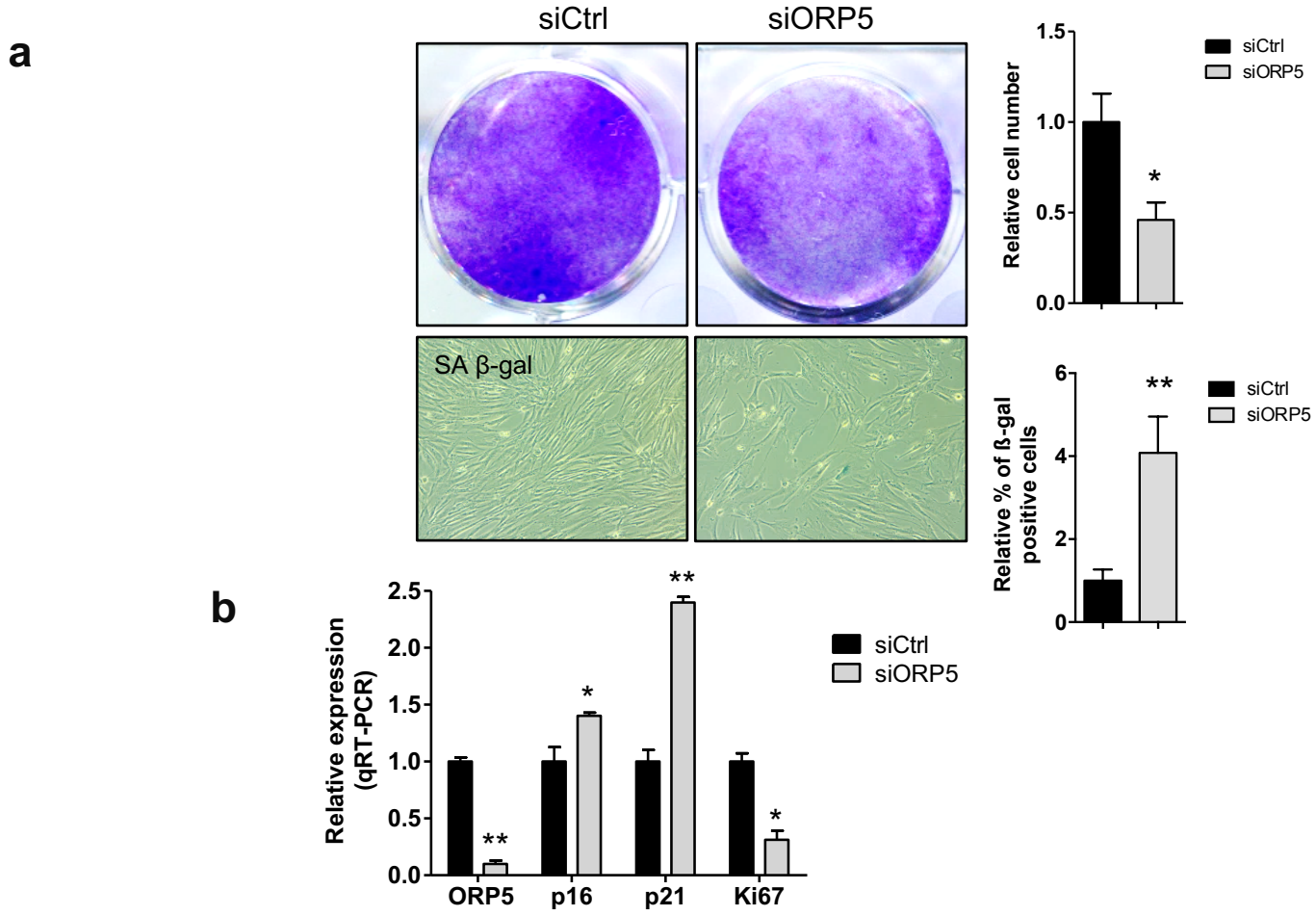
a
siCtrl
siORP5
SA β-gal
Relative cell number
1.5
1.0
0.5
0.0
*
siCtrl
siORP5
Relative % of ß-gal positive cells
6
4
2
0
**
b
Relative expression (qRT-PCR)
2.5
2.0
1.5
1.0
0.5
0.0
**
*
**
*
ORP5
p16
p21
Ki67

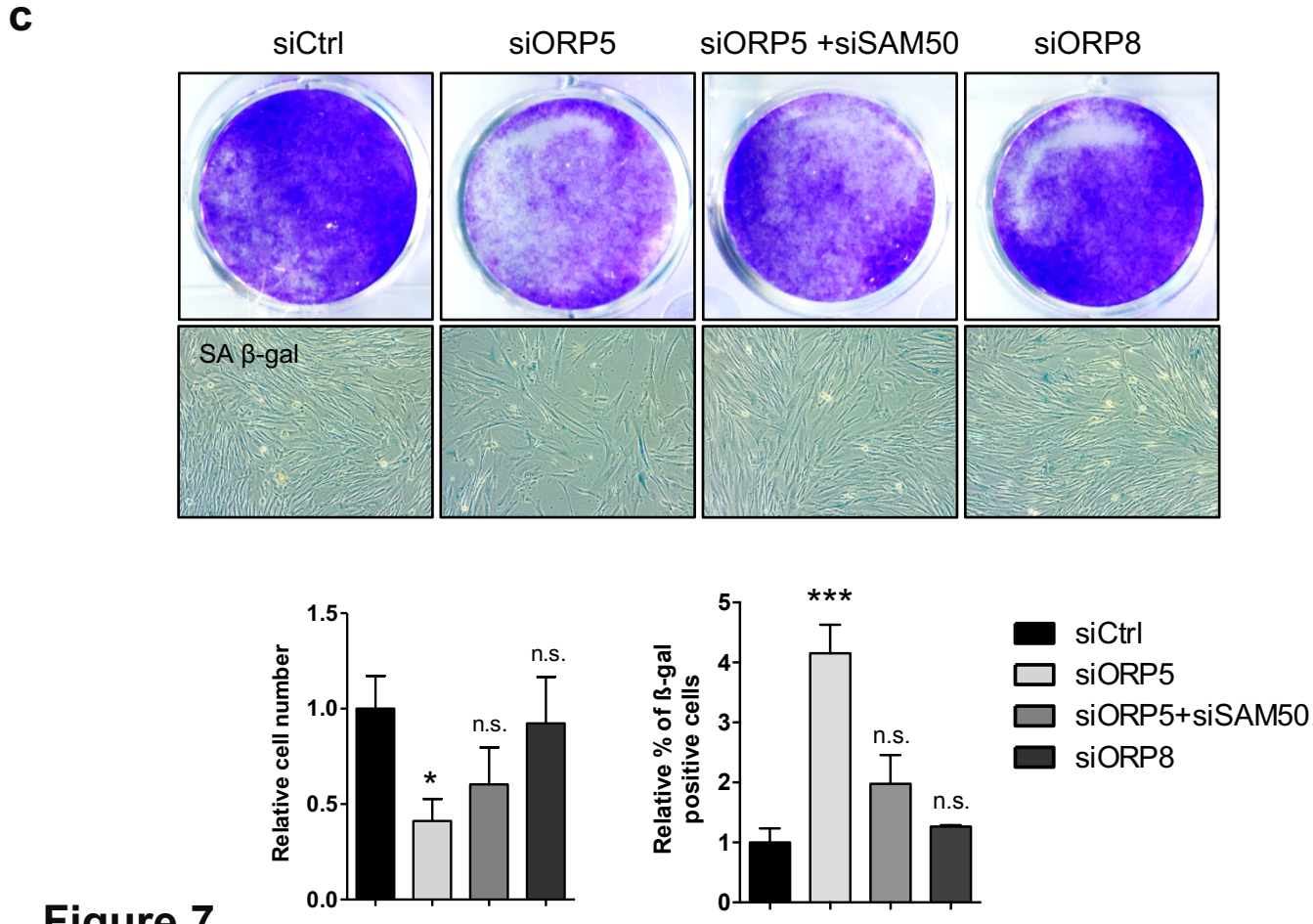
c
siCtrl
siORP5
siORP5 +siSAM50
siORP8
SA β-gal
Relative cell number
1.5
1.0
0.5
0.0
*
n.s.
n.s.
Relative % of ß-gal positive cells
5
4
3
2
1
0
***
n.s.
n.s.
siCtrl
siORP5
siORP5+siSAM50
siORP8

Figure 7

Figure 7. ORP5 knockdown promotes cell senescence

(a) MCR5 cells transfected with control siRNA or with siRNA against ORP5 were fixed and then stained with crystal violet solution (CA) or with SA-β-galactosidase (SA-β-Gal) staining solution. The graph on the top right shows the relative cell number determined by crystal violet staining. The graph on the bottom right shows the relative percentage of β-gal positive cells determined by SA-β-galactosidase assay. Data are presented as normalized mean ±SEM, n = 3 per condition, **, $p< 0.01$; *, $p< 0.05$. (b) Quantitative RT-PCR analysis of ORP5, p16, p21 and Ki67 in ORP5 knockdown cells and control HeLa cells. y axis:$2^{(-\Delta\Delta Ct)}$ value represents differences between the mean Ct (Cycle threshold) values of tested genes and those of reference genes (PGK1 and HPRT1). Data are presented as normalized mean ±SEM, n = 3 per condition, **, $p< 0.01$; *, $p< 0.05$. (c) MCR5 cells transfected with control siRNA or with siRNA against ORP5, SAM50 or ORP8 were fixed and then stained with crystal violet solution or with SA-β-Gal staining solution. The graph on the left shows the relative cell number determined by crystal violet staining. The graph on the right shows the relative percentage of β-gal positive cells determined by SA-β-galactosidase assay. Data are presented as normalized mean ±SEM, n = 3 per condition, ***, $p< 0.001$; *, $p< 0.05$; n.s; not significant.

a

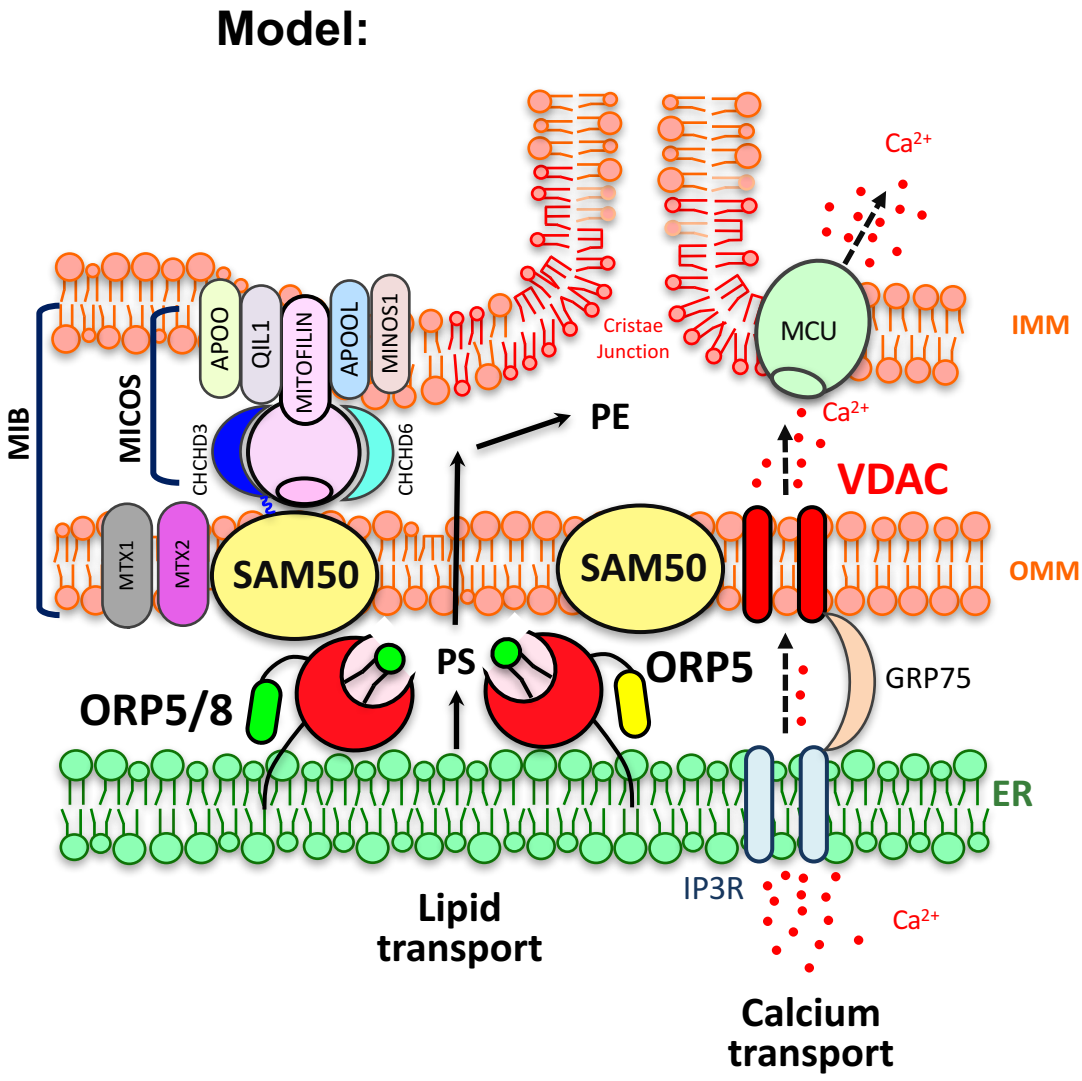

Figure 8. Lipid and calcium transport occur at the same ER-mitochondria contact site microdomains and are regulated by a ORP5-SAM50-VDAC pathway

ORP5/8 are directly involved in the transfer of PS from ER to mitochondria at ER-mitochondria membrane contact sites. This transfer occurs at the level of cristae junctions where ORP5/8 localize and interacts with the proteins of the MIB complex SAM50 and Mitofilin. This interaction facilitates the transfer of PS from ER to IMM at the level of the CJ where the PS is then converted into PE that play a critical role in cristae organization and mitochondrial function. ORP5 is also involved in calcium homeostasis by regulating the level of VDAC *via* SAM50 interaction and regulation.

Figure 8

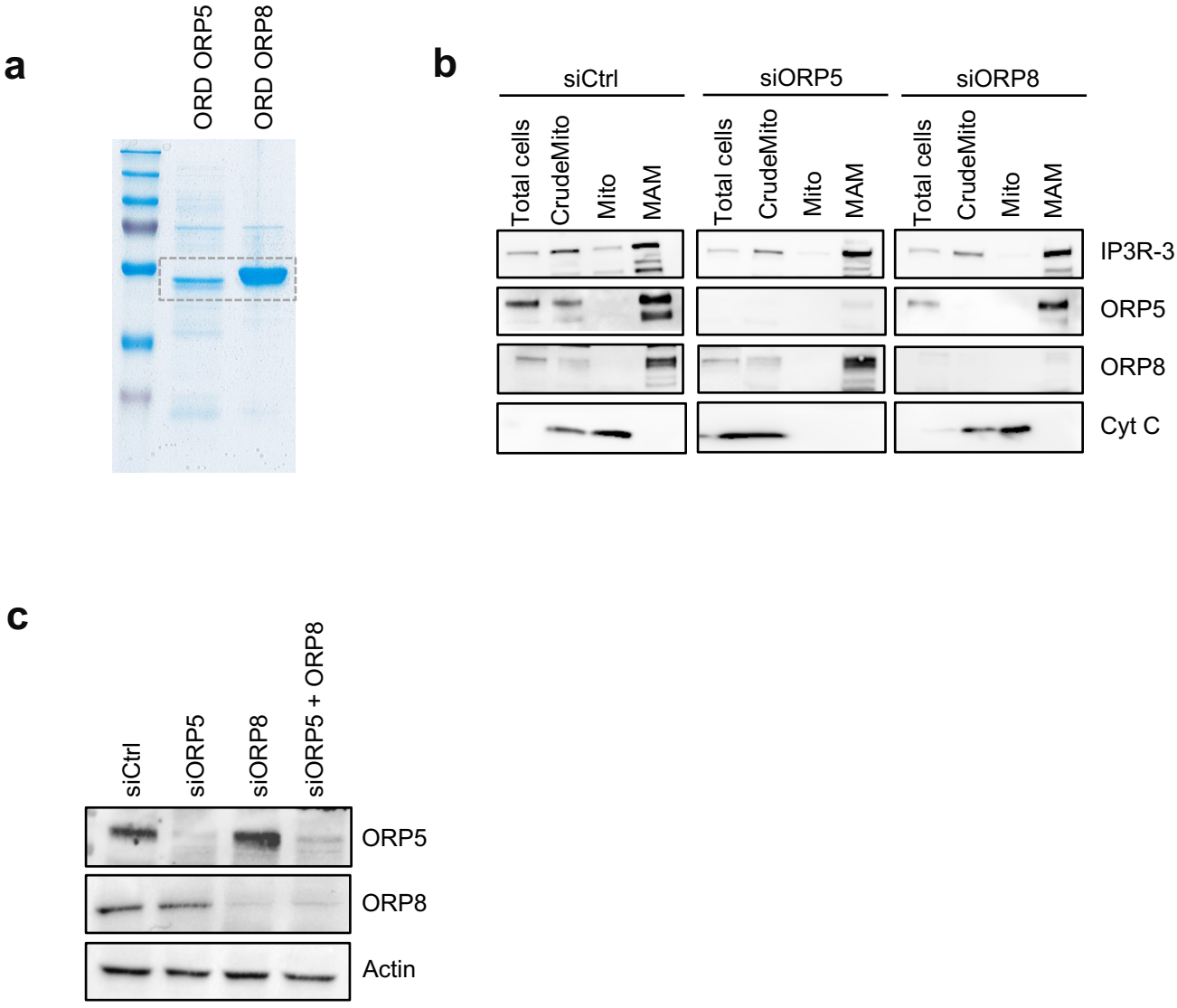

Figure S1. (a) Coomassie stained SDS-PAGE of the recombinant ORD domain of ORP5/8 proteins purified in BL21DE3 RILP cells. (b) Crude mitochondria, mitochondria, and MAM fractions were purified from Ctrl, ORP5 and ORP8 siRNA-treated HeLa cells. Equal amounts of protein from each fraction were loaded on a 4–20% gradient SDS–PAGE gel and immunoblotted using anti-ORP5, anti-ORP8, anti-IP3R-3 (MAM protein), and anti-cytochrome c (mitochondrial protein). Mito, mitochondria; MAM, mitochondria-associated ER membrane. (c) WB analysis showing ORP5, ORP8 and Actin levels in protein lysates from HeLa cells treated with either Ctrl siRNAs or with siRNAs against ORP5 or/and ORP8.

Figure S1

a

		IP EGFP	IP EGFP-ORP5	IP EGFP-ORP5ΔPH
Protein	**Localization**	**Mascot Score**		
ORP5	MAMs	0	9689	12192
ORP8	MAMs	31	930	690
Mitofilin	IMM	43	579	1150
SAM50	OMM	0	237	516
PSS1	MAMs	47	175	167
TOM22	OMM	0	77	95
PTPIP51	OMM	0	76	73
Metaxin2	OMM	0	32	175

b

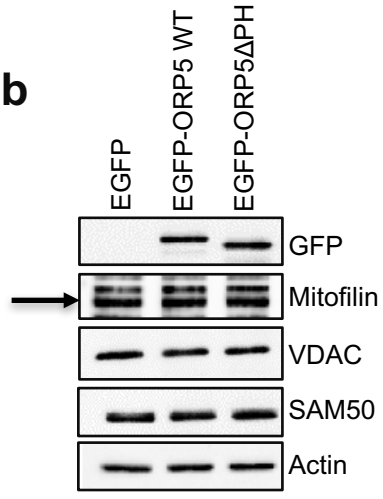

c

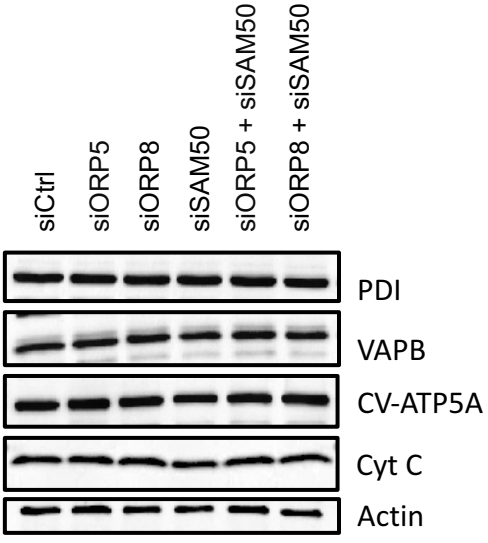

Figure S2. (a) Identification of proteins that interact with EGFP-tagged ORP5 constructs by mass spectrometry. Proteins associated to MAMs and mitochondrial outer and inner membranes (OMM, IMM) are interacting partners of EGFP-ORP5 constructs. Note the presence of some proteins of the MIB complex: Mitofilin, SAM50 and Metaxin2. The interaction of Mitofilin, SAM50 and Metaxin2 with the EGFP-ORP5ΔPH construct is stronger than with EGFP-ORP5. (b) WB analysis showing GFP (EGFP-tagged constructs), Mitofilin, VDAC and SAM50 and Actin levels in protein lysates from HeLa cells transfected with either EGF construct (Control) or with EGFP-ORP5 or EGFP-ORP5ΔPH constructs. (c) WB analysis showing PDI (ER), VAPB (ER), CV-ATP5A (IMM), Cytochrome C (Cyt C, IMM) and Actin levels in protein lysates from HeLa cells treated with either Ctrl siRNAs or with siRNAs against ORP5, ORP8, or SAM50.

Figure S2

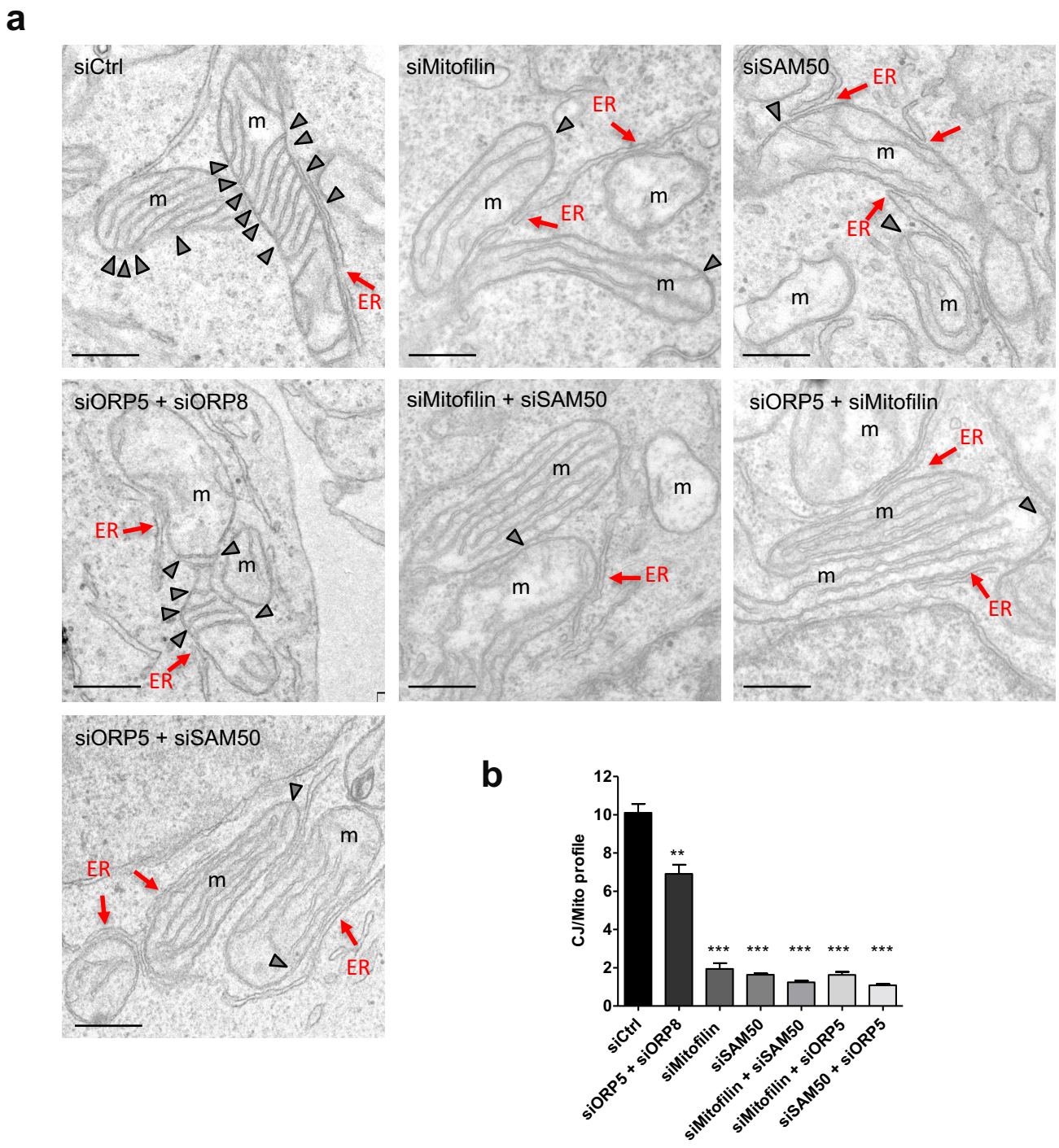

Figure S3. (a) Representative EM micrographs showing the morphology of mitochondria in HeLa cells treated with siRNA against ORP5, ORP8, Mitofilin and SAM50. Scale bar, 200 nm. Red arrows indicate ER elements in contact with mitochondria; arrowheads indicate CJ; m, mitochondria. (b) Quantifications of the number of CJ per mitochondria profile in the indicated siRNA conditions. % of CJ ±SEM, n = 170-260 mitochondria, ***, $p < 0.001$; **, $p < 0.01$.

Figure S3

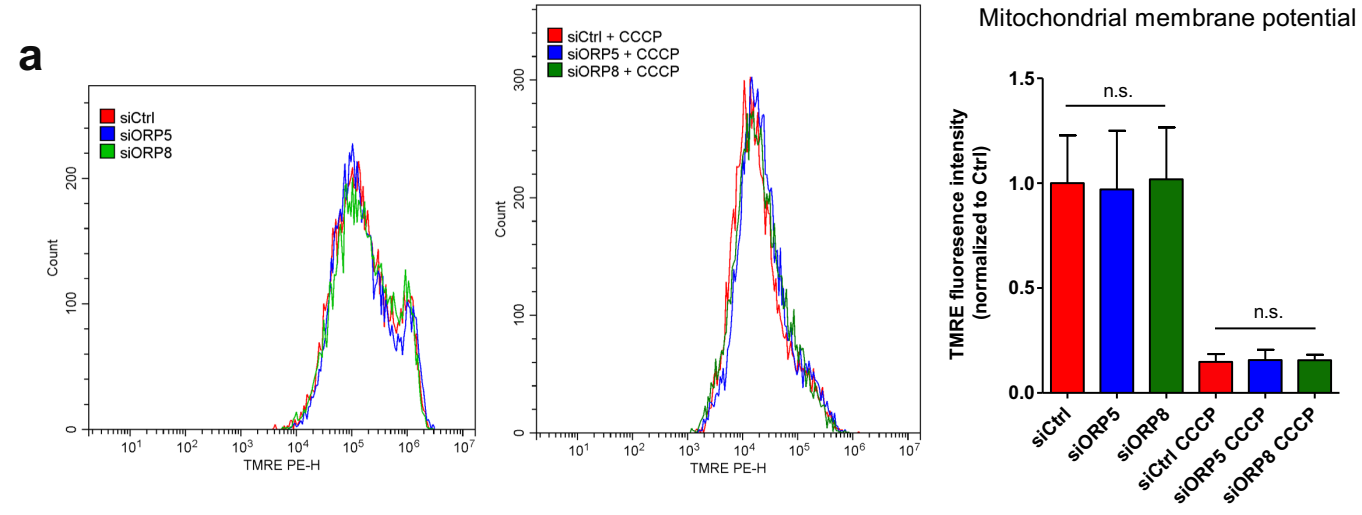
a
siCtrl
siORP5
siORP8
Count
TMRE PE-H
siCtrl + CCCP
siORP5 + CCCP
siORP8 + CCCP
Mitochondrial membrane potential
TMRE fluoresence intensity
(normalized to Ctrl)
n.s.
n.s.
siCtrl
siORP5
siORP8
siCtrl CCCP
siORP5 CCCP
siORP8 CCCP

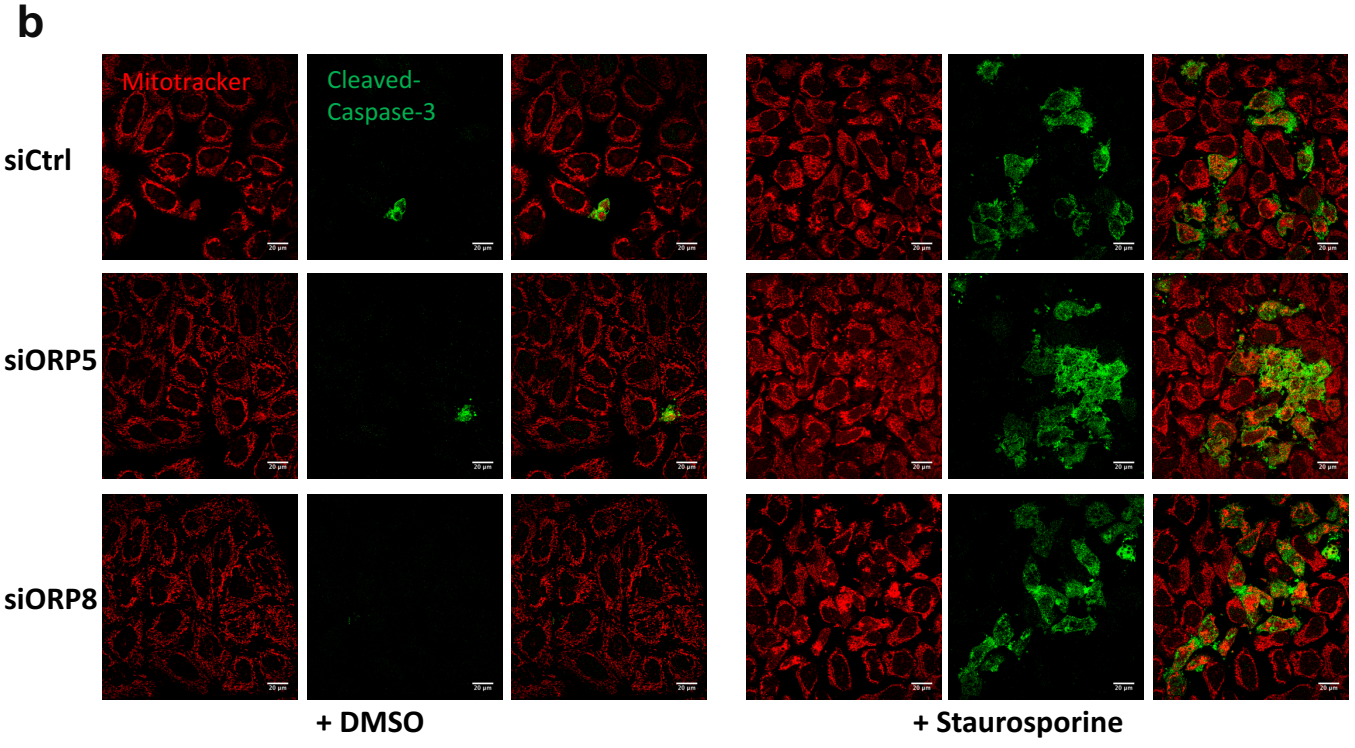
b
Mitotracker
Cleaved-
Caspase-3
siCtrl
siORP5
siORP8
+ DMSO
+ Staurosporine

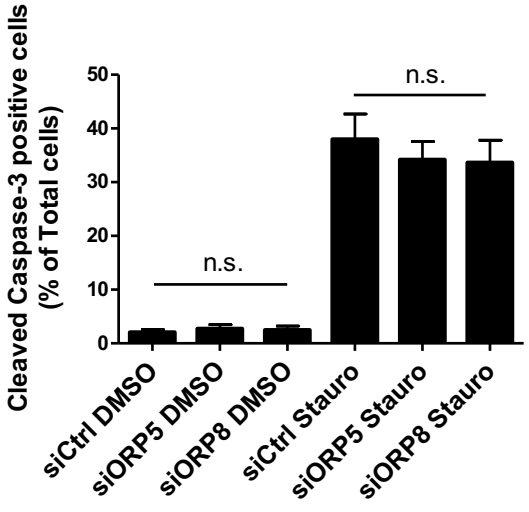
Cleaved Caspase-3 positive cells
(% of Total cells)
n.s.
n.s.
siCtrl DMSO
siORP5 DMSO
siORP8 DMSO
siCtrl Stauro
siORP5 Stauro
siORP8 Stauro

Figure S4

Figure S4. (a) Representative graphs of flow cytometry analysis of HeLa cells transfected with siRNA against ORP5 or ORP8 (n = 10 000 cells) and loaded with the mitochondrial membrane potential sensitive dye TMRE, in presence (right graph) or absence (left graph) of CCCP. Flow cytometry histograms are showing the relative TMRE fluorescence intensity; the average of three independent replicates is shown. Data are presented as normalized mean ±SEM. (b) Fluorescent images of HeLa cells transfected with siRNA against ORP5, ORP8 or control, treated with DMSO or staurosporine and stained with anti-cleaved Caspase-3 (apoptotic cells) and Mitotracker. Scale bar, 20 μm. The graphs represent the means ±SEM of the percentage of cleaved Caspase-3 positive cells in the different conditions; the average of three independent replicates is shown, n.s; not significant.